

ACCEPTED MANUSCRIPT

Coastal upwelling by wind-driven forcing in Jervis Bay, New South Wales: A numerical study for 2011

Sun Y-J., Jalón-Rojas, I., Wang, X.H., Jiang, D. (2018).

DOI

<https://doi.org/10.1016/j.ecss.2017.11.022>

Publication date

2018

Document version

Accepted author manuscript

Published in

Estuarine, Coastal and Shelf Science

Citation

Sun Y-J., Jalón-Rojas, I., Wang, X.H., Jiang, D. (2018). Coastal upwelling by wind-driven forcing in Jervis Bay, New South Wales: A numerical study for 2011. *Estuar. Coast. Shelf Sci.*, 206, 101-115, doi: 10.1016/j.ecss.2011.11.022

Important note

This is a PDF file of an unedited manuscript that has been accepted for publication. To cite this publication, please use the final published version (if applicable).

Please check the document version above in the following link:

<https://www.sciencedirect.com/science/article/pii/S027277141731096X>



This version of the accepted manuscript has been prepared according to the sharing policies of Elsevier: <https://www.elsevier.com/about/policies/sharing>

1 **Coastal upwelling by wind-driven forcing in Jervis Bay, New South Wales:**

2 **A numerical study for 2011**

3 Youn-Jong Sun^{1,3}, Isabel Jalón-Rojas^{1,*}, Xiao Hua Wang¹, Donghui Jiang²,

4 ¹ The Sino-Australian Research Centre for Coastal Management, School of Physical,

5 Environmental and Mathematical Sciences,

6 The University of New South Wales, Canberra, ACT 2600, Australia

7 ²Fisheries and Oceans Canada, Bedford Institute of Oceanography, Dartmouth, NS, Canada

8 ³Oceangraphic Inc. Seo-gu, Gwangju, 62060, South Korea

9 * Corresponding author: Isabel Jalón-Rojas, i.jalonrojas@unsw.edu.au

10 **Key points**

11 Behavior of cold bottom water intruded into Jervis Bay with varying wind directions

12 High impact of wind-driven upwelling on rate of water exchange

13 Effect of wind-driven downwelling within the bay

14 Wind-driven downwelling plays a key role in blocking the intrusion of the cold water

15
16 **Abstract**

17 The Princeton Ocean Model (POM) was used to investigate an upwelling event in Jervis Bay,

18 New South Wales (SE Australia), with varying wind directions and strengths. The POM was

19 adopted with a downscaling approach for the regional ocean model one-way nested to a

20 global ocean model. The upwelling event was detected from the observed wind data and

21 satellite sea surface temperature images. The validated model reproduced the upwelling event

22 showing the input of bottom cold water driven by wind to the bay, its subsequent deflection

23 to the south, and its outcropping to the surface along the west and south coasts. Nevertheless,

24 the behavior of the bottom water that intruded into the bay varied with different wind

25 directions and strengths. Upwelling-favorable wind directions for flushing efficiency within

26 the bay were ranked in the following order: N (0°; northerly) > NNE (30°; northeasterly) >

27 NW (315°; northwesterly) > NE (45°; northeasterly) > ENE (60°; northeasterly). Increasing
28 wind strengths also enhance cold water penetration and water exchange. It was determined
29 that wind-driven downwelling within the bay, which occurred with NNE, NE and ENE winds,
30 played a key role in blocking the intrusion of the cold water upwelled through the bay
31 entrance. A northerly wind stress higher than 0.3 N m^{-2} was required for the cold water to
32 reach the northern innermost bay.

33 **Keywords:** upwelling, downscaling approach, numerical model, alongshore wind, water
34 exchange, Jervis Bay

35 **1. Introduction**

36 Jervis Bay (JB) is a semi-closed embayment located on the east coast of Australia (35°
37 04'S, 150° 44'E; Fig.1). It has a north-south extent of 15 km, a west-east extent of 8 km, an
38 average depth of 15 m, and an area of 126 km². The width and depth of the bay entrance, are
39 3.75 km and 40 m, respectively (Wang and Symonds, 1999). The rate of water exchange with
40 offshore water is higher than in nearby bays, while nutrients and biological productivity are
41 lower (Joyce et al., 2010).

42 The marine environment of the JB has been exposed to pollutant problems from
43 anthropogenic development (Yamamoto, 2003; Anderson et al., 2008). Eutrophication is a
44 common phenomenon that has been frequently stimulated by nutrients such as phosphorus
45 and nitrogen released from rivers, ground water and catchment sewage systems. Because the
46 exchange rate between JB and offshore water is low, the accumulated pollutants within the
47 bay take a long time (10~74 days) to be flushed out varying with the tidal flow (Holloway et
48 al., 1992b). Furthermore, eutrophication events may lead to the occurrence of Harmful Algal
49 Blooms (HABs) within the bay, deteriorating water quality. Eutrophication can therefore
50 have an adverse impact on the marine ecosystem and limit human activities (e.g., leisure
51 sports and tourism).

52 Given the above, coastal upwelling events in Jervis Bay can play an important role,
53 not only in flushing out nutrient material accumulated in the bay, but also in importing
54 nutrients into the bay from offshore water and therefore in producing algal blooms; this is all
55 the more so because river inflows into JB (e.g., Currambene Creek, Callala Creek, and
56 Moona Moona Creek) are negligible (Blackburn and Cresswell, 1993; Kai et al., 1999; Oke
57 and Middleton, 2001; Pritchard et al., 2003; Lee et al., 2007; Anderson et al., 2008; Trainer et
58 al., 2000). Understanding the coastal upwelling intrusion into JB is therefore a key, but still
59 poorly investigated, research and management challenge.

60 The influence of East Australian current (EAC) and its eddies on the hydrographic
61 properties of this area is instead well known. The EAC flows poleward off the east coast and
62 separates around Sugarloaf Point (32.4°S), which is where it typically generates anticyclonic
63 warm core eddies. In summer, it can advect warm surface waters down to Tasmania. The
64 Tasman Front forms the interface between the warm Coral and the cool Tasman Seas (Fig.
65 1a). At times, baroclinic Rossby waves triggered by oscillations of the Tasman Front travel
66 toward the east coast of Australia, producing a small cold-core (cyclonic) eddy (Marchesiello
67 and Middleton, 2000). Since the cold water from the Tasman Sea approaches the bay
68 entrance, the formation of eddies near the bay mouth affects the circulation within the bay
69 (Holloway et al., 1991; Joyce et al., 2010). Aside from the EAC, density driven currents, tidal
70 processes, and coastal trapped waves (CTW) influence circulation patterns. During the
71 summer season, bay circulation is dominated by sub-inertial baroclinic flows that are created
72 as a baroclinic response of the bay to the scattering of CTWs in the form of internal Kelvin
73 waves (Middleton, 1994; Wang and Wang, 2003).

74 In JB, the M_2 semi-diurnal tidal current is dominant but weak, with a speed of 0.02 m
75 s^{-1} (Holloway et al., 1992b). Accordingly, circulation and shelf upwelling intrusion are the
76 main physical mechanisms. In particular, it is worth determining how coastal upwelling on

77 the shelf intrudes into the bay and how this intrusion varies with time and space. It is known
78 that coastal upwelling near JB is mainly driven by two factors: 1) the warm EAC and its
79 eddies (Tranter et al., 1986; Huyer et al., 1988; Holloway et al., 1992a; Blackburn and
80 Cresswell, 1993; Hallegraeff and Jeffery, 1993); and 2) upwelling-favorable winds (Smith,
81 1968; Lewis, 1981; Rochford, 1984; Schahinger, 1987). In the southern hemisphere, winds
82 blowing in a poleward direction along a western boundary tend to cause upwelling.
83 Alongshore currents (Huyer et al., 1988; Gibbs et al., 1997) and bottom Ekman-transport
84 convergence (Herzfeld and Tomczak, 1999) are considered to be minor factors driving
85 upwelling events along the east and south coasts of Australia.

86 Although upwelling can be driven by onshore encroachment of the EAC near the
87 Sydney shelf (McClellan-Padman and Padman, 1991; Roughan and Middleton, 2004), wind-
88 driven upwelling is more significant (Gibbs et al., 1997; Marchesiello and Middleton, 2000).
89 This has been confirmed by analysis of NOAA-11 remote Sea Surface Temperature (SST)
90 images (Gibbs et al., 1997) and by numerical analysis (Marchesiello and Middleton, 2000).
91 Meanwhile, Gibbs et al. (1998) suggested that the formation of baroclinic instability by the
92 EAC off the east coast of Australia prior to upwelling-favorable winds could more actively
93 trigger coastal upwelling. Nevertheless, it is presumed that upwelling-favorable wind is the
94 primary forcing mechanism driving upwelling in JB and plays an important role in
95 transporting nutrients to the coast and into the bay (García-Reyes and Largier, 2010).
96 However, various aspects are still not well understood, including how wind-driven upwelling
97 affects the bay circulation and the water exchange between the open sea and JB, and the
98 variability of upwelling intrusion with varying wind direction and strength.

99 This study first aims to establish a validated bay model and then to investigate how JB
100 responds to wind-driven coastal upwelling on its shelf, and how the water exchange and
101 flushing rates of the bay vary with wind direction and strength. Model description is provided

102 in Section 2. Section 3 describes the observations used to detect wind-driven coastal
103 upwelling and to validate the model, as well as the methodology used to assess residence
104 times. Section 4 presents model results, together with model validation. Finally, Sections 5
105 and 6 discuss wind-driven upwelling and its variability with wind direction and strength.

106 **2. Model Descriptions**

107 The Princeton Ocean Model (POM; Mellor, 2004) was used with a downscaling
108 approach (Oddo and Pinardi, 2008) for a regional ocean model (hereafter referred to as the JB
109 model). The JB model is one-way nested into a global ocean model: the Ocean Forecasting
110 Australian Model (OFAM; Schiller et al., 2008). OFAM is first introduced in Section 2.1,
111 while the JB model configuration is described in Section 2.2. Methods to nest boundary
112 conditions between the global ocean model and the JB model are outlined in Section 2.3.

113 **2.1. The Ocean Forecasting Australian Model**

114 The Ocean Forecasting Australian Model (OFAM) has underpinned the Bluelink
115 ReANalysis - version 2p1 (BRAN2; Oke et al., 2013), a multi-year integration of OFAM for
116 the last few decades, along with the Bluelink Ocean Data Assimilation System (BODAS; Oke
117 et al., 2008). BLUElink, which is an Australian partnership between the Commonwealth
118 Scientific and Industrial Research Organization (CSIRO), the Bureau of Meteorology (BoM),
119 and the Royal Australian Navy (RAN), has produced the Ocean Modeling, Analysis, and
120 Prediction System - version 1.0 (OceanMAPS1; Brassington et al., 2012). This operational
121 system used for short-term forecasting is also underpinned by OFAM and BODAS. Data for
122 variables such as temperature, salinity, velocity, and sea surface forcing (wind stress and heat
123 flux) were extracted from BRAN2 and OceanMAPS1 in order to force the JB model.

124 Based on the Modular Ocean Model (version 4; MOM4), OFAM has a vertical
125 resolution of 47 levels at constant 10 m intervals from the sea surface to 200 m depth. The
126 vertical spacing increases then exponentially with depth from 200 m below the surface. The

127 surface forcing of BRAN includes the European Centre for Medium-Range Weather
128 Forecasts (ECMWF) for wind stress, heat, and fresh water fluxes. Satellite and in situ
129 oceanographic data were also all assimilated into BRAN (Oke et al., 2008). In the case of the
130 open ocean, BRAN currents were corrected with ocean surface topography from satellite
131 altimeters and coastal tidal gauges, complemented by a mean dynamic height field derived
132 from historical observations (Schiller et al., 2008). The BLUElink forecasting system was
133 developed in OceanMAPS (Brassington et al., 2007) and was implemented operationally in
134 August 2007 to provide routine real-time ocean analysis and forecasts and/or reanalysis
135 products (Dombrowsky et al., 2009). Further details about BRAN and OceanMAPS are
136 provided in the following works: Brassington et al. (2007), Schiller et al. (2008), Oke et al.
137 (2008), Dombrowsky et al. (2009), Brassington et al. (2012), Oke et al. (2013), Wang et al.
138 (2013), and Wang et al. (2015).

139 **2.2. Jervis Bay model configuration**

140 For the JB model, hydrostatic and Boussinesq approximations were used with the
141 composite of ETOPO1 (National Geophysical Data Centre, Boulder, Colorado) and a high
142 resolution (100 m \times 100 m) JB bathymetry provided by the RAN. The model grid has 234 \times
143 258 horizontal points in x and y directions, with finer cells (about 500 m) around JB and
144 coarser cells (about 7 km) in open boundaries (x : 438 ~ 7403 m, y : 556 ~ 6922 m). Twenty-
145 one sigma levels were used in the z direction, with finer layers near the surface and bottom.
146 The Smagorinsky diffusivity was used for horizontal viscosity and diffusivity, and the
147 turbulence closure scheme described by Mellor and Yamada (1982) was adopted for vertical
148 mixing coefficients. Surface forcing from BRAN2/OceanMAPS1, such as heat flux and wind
149 stress, was introduced into the JB model domain. The four major tidal forcings (M_2 , S_2 , O_1 ,
150 and K_1), which were calculated from NAO.99b (Matsumoto et al., 2000), were given along
151 lateral open boundaries. Daily mean temperature, salinity, and currents (u and v) provided by

152 BRAN2/OceanMAPS1 were used to force the JB model. The time intervals chosen for
153 external and internal modes were set at 0.2 s and 12 s, respectively, satisfying the Courants-
154 Friedrichs-Lewy (CFL) condition. Appropriate downscaling techniques were developed or
155 adopted for one-way grid nesting of the regional model to the global ocean model. The
156 performance of the regional model depended on how well this nesting was handled.

157 **2.3. Open boundary condition - scale selective approach**

158 Nesting temperature and salinity fields between the global ocean model and the JB
159 model along its northern open boundary was critical for model performance. The Sommerfeld
160 (1949) Radiation Condition and the Scale Selective Approach (SSA; Oddo and Pinardi, 2008)
161 were applied in the southern and eastern open boundary and in the northern open boundary,
162 respectively. SSA was applied only in the northern open boundary because the EAC inflow
163 controls circulation and water exchange between JB and adjacent shelf ocean water
164 (Marchesiello and Middleton, 2000). The SSA solved the temporal and spatial resolution
165 inconsistency between the JB model and the global model at the open boundary, and removed
166 numerical instability within the model. The nested model was separated into two fields, as
167 follows (Oddo and Pinardi, 2008):

$$168 \quad \theta_f = \theta_f' + \theta_f'' \quad (1)$$

169 where θ_f' is the global field, which is the part of the solution pertaining to the overlapping
170 spectral window between nesting (coarser) and nested (regional) models, and θ_f'' is the
171 regional field, which is the specific component of the nested model. Equation 1 was redefined
172 by replacing θ_f with θ^{ext} at the lateral open boundary, where θ^{ext} is either observation data
173 or coarser model outputs. This is often used in one-way nesting (Oddo and Pinardi, 2008). By
174 obtaining θ_f'' and applying it to the lateral open boundary, we were able to obtain a better
175 result than the regional model in which a standard radiation open boundary condition was

176 applied (Perkins and Smedstad, 1998; Oddo and Pinardi, 2008). This nesting scheme was
177 applied to the JB regional model for heat, salinity, and volume transport at the open boundary.

178 **3. Methods and materials**

179 **3.1 Wind and satellite data**

180 Wind stress data and satellite SST images were used to identify upwelling events off
181 the east coast of Australia. Observed wind data are taken from Pt. Perpendicular Automatic
182 Weather Station (AWS) which is located at the northern entrance to Jervis Bay (Fig. 1c).
183 Modeled wind forcing data are extracted from OceanMAPS. In terms of satellite data, Group
184 for High Resolution Sea Surface Temperature (GHRSSST) Level 4 sea surface temperature
185 analysis was provided by the BoM through a real-time, high-resolution, Regional Australian
186 Multi-Sensor Sea surface temperature Analysis (RAMSSA) system ([http://podaac-](http://podaac-opendap.jpl.nasa.gov/opendap/allData/ghrsst/data/L4/AUS/ABOM/RAMSSA_09km/2011/contents.html)
187 [opendap.jpl.nasa.](http://podaac-opendap.jpl.nasa.gov/opendap/allData/ghrsst/data/L4/AUS/ABOM/RAMSSA_09km/2011/contents.html)
188 [gov/opendap/allData/ghrsst/data/L4/AUS/ABOM/RAMSSA_09km/2011/contents.html](http://podaac-opendap/allData/ghrsst/data/L4/AUS/ABOM/RAMSSA_09km/2011/contents.html)). The
189 RAMSSA system produces daily SST using optimal interpolation (OI) at a $1/12^\circ$ resolution
190 over the Australian region (20°N – 70°N , 60°E – 170°W).

191 **3.2. Hydrographic observations**

192 Historical observations (June 26, 1998) of water temperature and currents were used to
193 validate the JB model. The CTD (Neil Brown ‘Smart’) survey was conducted between 08–14
194 h on June 26, 1998 (Thomas, 1998). ADCP (Broadband; 614.4 kHz with bin size = 1 m) data
195 were collected during the CTD survey. ADCP tracks (*a-e*) and CTD stations for June 26,
196 1998 are shown in Fig. 3a. The downward-looking ADCP was attached to the side of the
197 research vessel TARKA. Data were averaged at 400 m intervals along each track. Observed
198 data for the validation of temperature for 2011 were also obtained from thermistors (SBE 39;
199 sampling rate = 5 min) deployed at three points (T1, T2, and T3; see Fig. 1c) within JB from
200 March to August 2011. Data were filtered by hourly moving average.

201 3.3. Methodology to describe the water exchange

202 Eulerian passive tracers were used to assess the impact of wind-driven upwelling on
203 water exchange under different scenarios of wind direction and strength. We used the
204 definition of “local flushing time” or “local residence time” proposed by numerous works,
205 such as Abdelrhman, (2005), Plus et al. (2009), Cucco et al. (2009) and Grifoll et al. (2013).
206 Following these works, a Eulerian passive tracer with a concentration equal to 1 was
207 deployed at each grid point (i) within the inner domain of the bay at time t_0 . No further
208 amount of the tracer is added into the bay after t_0 , and the volume (V) on each grid of the bay
209 remains constant over time. The concentration of tracers at each grid point (C_i) evolves with
210 time (t) as bay water is exchanged with the open ocean at a change rate defined as:

$$211 \quad CR(t) = \frac{\sum_{i=1}^n C_i(t)V_i(t)}{\sum_{i=1}^n C_i(t_0)V_i(t_0)} \quad (2)$$

212 where the subscript i is each grid point within the bay. The global residence or
213 flushing time of the bay was calculated as the time for which the tracer mass contained
214 initially in the domain falls below e^{-1} (37%), i.e. the time required to reduce the change rate
215 CR by 63%. Similarly, the spatial distribution of the residence time was obtained as the time
216 required in each horizontal water parcel for the depth-averaged tracer concentration to fall
217 below 37% of the initial depth-averaged concentration.

218

219 4. Results

220 4.1. Wind-driven coastal upwelling detected in the satellite images

221 The satellite images for the period March 18-26, 2011 (Figs. 2a and 2b) show that the
222 upwelling event occurred along the coast of JB from March 20–22, as indicated by local
223 upwelling-favorable wind stresses (see the ellipses in Figs. 2c and 2d). When strong
224 upwelling carries deep ocean water with low temperature, high salinity and nutrients to the
225 coast, it can result in the formation of an SST front, which may be evident in satellite SST

226 images (Marcello et al., 2005). The appearance of abnormally low temperatures at the sea
227 surface and in subsurface water indicates the occurrence of upwelling events (Hu et al., 2001).

228 During upwelling events, cold water outcropping along the coast of JB is clearly
229 evident in the SST satellite image, as shown within the red ellipses in Figs. 2a and 2b. SST
230 distributions along the coast during the three days (March 21, 2011) after the beginning of the
231 upwelling-favorable wind (March 18, 2011) clearly show that cold water appeared at the
232 surface on this occasion.

233 **4.2. Observation and numerical results for validation**

234 Only June 1998 was selected for model validation as this was the period during which
235 observations for ADCP and CTD data were carried out horizontally and vertically over the
236 whole JB area (Fig. 1c, Section 3.2). This validated model was then used to predict the wind-
237 driven upwelling detected in the satellite images (Figs. 2a and 2b) during March 18-26, 2011.
238 First, to validate the tidal components of the model within the bay, the Root Mean Square
239 (RMS) difference between the model and observations was computed, as follows [Masson
240 and Cummins, 2004]:

$$241 \quad D = \sqrt{\frac{1}{2}(A_m^2 + A_o^2) - A_m A_o \cos(\phi_m - \phi_o)} \quad (3)$$

242 where A and ϕ are tidal amplitude and tidal phase, respectively. Subscripts m and o indicate
243 the model and observation, respectively. Table 1 shows absolute differences between
244 observation and model results for each tidal constituent used to force the model for the year
245 1998. The maximum difference in amplitude and phase of four tidal constituents for 1998 is
246 less than 5.1 cm and $\pm 2.0^\circ$. As stated in Section 1, observation and model tidal level results
247 for 1998 at the station Tg (Figure 1c) reveal that the tidal effect in JB is weak, even though
248 M_2 , the semi-diurnal tide, is dominant [Holloway et al., 1992b]. Accordingly, it is presumed
249 that the difference between observations and model results for tidal constituents has little
250 effect on circulation within JB.

251 The current velocity field from observations (between 08–14 h) and daily-averaged
252 model results for June 26, 1998 shows a two-layer flow, with the surface flowing to the
253 southwest and bottom currents flowing to the northeast of the bay (Figs. 3a-3d). The current
254 vectors of Transects *a* and *b* at the surface (Figs. 3a and 3c) show a northward flow on the
255 western side and a southward flow on the eastern side, forming a clockwise circulation, while
256 a distinct southward flow along the eastern boundary can be seen at the bottom (Figs. 3b and
257 3d). As shelf water enters the bay beyond the entrance (observed/modeled), it is deflected to
258 the south, with the strongest currents ($20 \text{ cm s}^{-1}/14 \text{ cm s}^{-1}$) occurring in the center of the
259 southern basin (Transects *c* and *e* in Fig. 3a). The current pattern across the entrance of JB
260 (Transect *e*) for observed (modeled) results showed a predominant inflow and outflow at the
261 surface and bottom, with velocities of 15 cm s^{-1} (10 cm s^{-1}) and 11 cm s^{-1} (9 cm s^{-1}),
262 respectively. Surface current vectors for observation and model results hence showed
263 anticlockwise circulation in the southern basin and weak clockwise circulation in the northern
264 basin. This circulation was forced by the atmospheric cooling event within JB in the winter
265 season, as already described by Wang and Symonds (1999).

266 Tidal currents computed by the JB model align with the channel axis owing to the
267 strong influence of topography on current direction (not shown). The tidal current for M_2 was
268 predicted to have a velocity of 0.1 m s^{-1} at the entrance, and smaller values of 0.02 m s^{-1}
269 within the bay. These correspond to about 0.07 m s^{-1} and less than 0.01 m s^{-1} measured at the
270 entrance and northern side of JB, respectively, by Holloway et al. (1991).

271 The horizontal distribution of temperature and salinity are also used to validate the JB
272 model. Temperature observations between 08–14 h and daily-averaged model results for June
273 26, 1998 are compared in Figs. 3e and 3f. The distribution of surface temperature
274 (observation/model) showed the presence of warm water ($18.4^\circ\text{C}/18.0^\circ\text{C}$) at the entrance of
275 the bay (Figs. 3e and 3e'). The distribution of bottom temperature revealed that warmer water

276 at the bottom penetrated into the bay at the southern side of the bay entrance (Figs. 3f and 3f').
 277 The observed/modeled salinity distribution showed almost identical patterns to those of
 278 temperature distribution. The difference between observed and modeled maximum and
 279 minimum salinity values was only 0.38 psu and 0.03 psu, respectively (not shown). This was
 280 contrasted with a larger temperature difference of almost 3.0°C/4.0°C for the observed-
 281 modeled maximum and minimum, respectively. The density distribution was similar to the
 282 temperature pattern (not shown). Least dense water occurred at the entrance and dominated
 283 the south-east region. The southern side mainly consisted of less dense water that penetrated
 284 marginally into the bay. The model for June 1998 successfully reproduced the observed
 285 finding that the vertical temperature gradient from the inner bay (Callala) to the entrance
 286 (Bowen Island) was tilted towards the inner bay with a difference of 2°C (Figs. 3g and 3g')
 287 while the temperature gradient of the vertical section along the bay entrance had a 2.5°C
 288 slope toward Dart Point (Figs. 3h and 3h'). As cold bottom water flowed out of the bay, it
 289 was replaced by warm surface inflow (Figs. 3g, 3h, 3g' and 3h').

290 Furthermore, model performance on the shelf and in open-ocean was validated by
 291 yielding a correlation coefficient between modeled and observed (Advanced Very High
 292 Resolution Radiometer, AVHRR) anomalies from the climatological SST value (CARS2009),
 293 as follows (Krishnamurti et al., 2003, Wang et al., 2013):

$$294 \quad ACC = \frac{\sum_{i=1}^N \{[(F_i - C_i) - \overline{(F_i - C_i)}][A_i - C_i - \overline{(A_i - C_i)}]\}}{\sqrt{\sum_{i=1}^N [(F_i - C_i) - \overline{(F_i - C_i)}]^2 \sum_{i=1}^N [A_i - C_i - \overline{(A_i - C_i)}]^2}} \quad (4)$$

295 where F is modeled, C is climatology, and A is observed value (AVHRR) for SST. The
 296 suffixes (i) indicate each grid point. The Anomaly Correlation Coefficient (ACC) analysis
 297 measures the spatial similarity between modeled results and observed data for large regions.
 298 Using Eq. 4, we found that the ACC value was 0.7 for June 1998. In general, an ACC value of
 299 0.6 is regarded as the limit for useful validation. Moreover, it was revealed that the root mean

300 squared error (RMSE) of SSTs between observed data and modeled results over the whole
301 domain was about 1°C for the period in question.

302 **4.3. Numerical results for the wind-driven coastal upwelling in March, 2011**

303 As mentioned in section 1, coastal upwelling near JB could be driven by the EAC and
304 by upwelling-favorable winds. Nevertheless, it was hypothesized that the latter could have
305 been the primary force driving upwelling into the bay in 2011, as identified from satellite data
306 (Fig. 2). This coastal upwelling event would hence be reproduced by the JB model during the
307 period from March 18–26, 2011, when upwelling-favorable winds had blown consistently as
308 described in previous sections.

309 Reproducing the upwelling event during the period from March 18-26, the
310 distribution of SST on March 20, 2011 is clearly divided into the southern and northern part
311 of the bay by the 22°C isotherm (Fig. 4a). The SST of the northern side is cooler than of the
312 southern side. On March 24, when the local wind began turning westerly, cold water lower
313 than 21°C outcropped to the surface along the west and south coasts of JB , indicating a
314 progressive upwelling event (Fig. 4c). Consequently, the north-south SST gradient in the bay
315 was reversed (Fig. 4d).

316 The cold bottom water (taking the 18°C contour as an indicator) began to intrude into
317 the bay through the entrance on March 21 (Fig. 4b'); on March 23, the cold bottom water
318 reached the middle of the bay (Fig. 4c'). From March 24, the cold water deflected to the
319 southern part and occupied the middle to southern part of the bay (Fig. 4d'). Bottom
320 temperature of the southern part became therefore 2°C lower than in the northern part.

321 The horizontal distribution of temperature (Fig. 4) shows therefore how upwelling
322 occurs in JB. In addition, observed surface and bottom temperatures at three stations (Figs. 4e
323 and 4f) were plotted for the specific period from March 18–26, 2011. The upwelling event
324 started to appear only at the bottom of T1 from March 21 and on March 23, 2011, and the

325 coldest water intruded with tidal oscillation through the bay entrance (Fig. 4f). However, T2
 326 and T3 were not affected by the upwelling event because this did not extend to the northern
 327 part of the bay (Figs. 4a'-d').

328 **4.4 Coastal upwelling variations related to wind direction and strength**

329 As revealed through the model results in section 4, the response of the bay to the
 330 upwelling events varied with wind direction and strength. In order to investigate how wind-
 331 driven coastal upwelling affects the temperature field within JB and the ocean-bay water
 332 exchange under different wind conditions, we carried out two numerical experiments to
 333 simulate an upwelling event over a two-week period based on five and seven different wind
 334 directions and strengths, respectively (Table 2). These experiments with the prolonged period
 335 of wind forcing allow the passive tracer experiments to be completed for residence times. The
 336 first experiment consists of five different simulations from March 18 to April 4 characterized
 337 by a constant wind strength, 0.4 N m^{-2} , and different upwelling-favorable wind directions:
 338 NNE (30° clockwise from the north), ENE (60°), NE (45°), N (0°), and NW (315°). The
 339 second experiment includes seven simulations from March 18 to April 4 with a constant
 340 upwelling-favorable NNE (30°) wind direction and varying wind strengths (from 0.05 to 0.5
 341 N m^{-2} , Table 2). Wind stress, τ (N m^{-2}), given by local surface forcing of the JB model, was
 342 calculated as per the following equation (Pond and Pickard, 1983):

$$343 \quad \tau = \rho_a C_d V^2 \quad (5)$$

344 where V (m s^{-1}) is wind speed; ρ_a (kg m^{-3}) is air density; and C_d is a drag coefficient yielded
 345 by Trenbreth et al. (1990) as follows:

$$346 \quad C_d = 10^{-3} \times \begin{cases} 0.49 + 0.065V & \text{for } V > 10 \text{ m s}^{-1} \\ 1.14 & \text{for } 3 \text{ m s}^{-1} \leq V \leq 10 \text{ m s}^{-1} \\ 0.62 + 1.5V^{-1} & \text{for } V \leq 3 \text{ m s}^{-1} \end{cases} \quad (6)$$

347 In all the experiments, only wind forcing for the JB region (150.54–150.99°E and, 34.91–
348 35.23°S) was given. A third experiment (no wind, Table 2) that did not consider wind effects
349 was also undertaken to examine only the effect of the EAC on coastal upwelling.

350 First, the intrusion of wind-driven upwelling into JB was analyzed from the daily
351 mean temperature and the horizontal distribution of current vectors on March 21 for the
352 different experiments. The calculation of residence times for the different scenarios of wind
353 gives then an insight on the impact of wind-driven upwelling on the rate of water exchange.

354 **4.4.1. Impact of wind conditions on upwelling intrusion**

355 Daily averaged surface and bottom temperature and velocity were simulated with
356 varying wind directions (Fig. 5). In the cases of NNE, ENE, and NE winds, bottom water
357 (18°C isotherm in the right panels of Fig. 5) penetrated along the eastern boundary of the bay,
358 but its intrusion distance (along the center axis of the 18°C isotherm starting from the middle
359 of the bay entrance) varied with wind directions in the following order: NNE (9.2 km) > NE
360 (7.8 km) > ENE (6.5 km). Under a northerly wind (N), cold bottom water approached the
361 innermost bay (9.7 km) and outcropped on the surface (Figs. 5d and 5d'). Strong bathymetric
362 control of flow in response to wind forcing was also observed. The northwesterly (NW) wind
363 led to cooler water in the western part (8.4 km) of the bay (Figs. 5e and 5e'). As cold water
364 came into the entrance, it was deflected to the southern part of the bay, with strong currents
365 occurring in the center of the southern basin in most cases after March 21 (not shown). The
366 horizontal distributions of current vectors at the surface show downwind flows, while at the
367 bottom, flow patterns vary with wind direction. The NNE, ENE, and NE winds concurrently
368 lead to flows along the eastern coast of the bay and from west to east. The northerly (N) wind
369 caused cold water to penetrate across the center of the bay. The NW down-estuary wind
370 formed an upstream flow within the bay. Interestingly, middle layer horizontal distribution of

371 current vectors formed an anticyclonic eddy with elliptical shape, elongated along the
372 western part of the bay; the exception was the NW (not shown).

373 Figure 6 shows the distributions of daily-averaged surface and bottom temperatures
374 simulated with varying wind strengths. The EAC without wind on bottom cold water affected
375 the area around the bay entrance and its effect disappeared after March 21 (not shown). At
376 the surface, the circulation formed an anticyclonic eddy due to the baroclinic response of the
377 bay to the scattering of CTWs in the form of internal Kelvin waves (Middleton, 1994; Wang
378 and Wang, 2003). In the case of wind with magnitude of 0.1 N m^{-2} or less, bottom cold water
379 (not shown in the case of 0.05 N m^{-2}) tended to deflect toward the southern part of the bay,
380 though it in part penetrated along the eastern coast. As wind strength increased, bottom water
381 moved along the eastern boundary of the bay and further approached the innermost area. Also,
382 with high wind strengths, the cool temperature (21°C) in the northern part broadly extended
383 along the eastern coast. However, the behavior of bottom water generated by wind $\geq 0.3 \text{ N m}^{-2}$
384 made no great difference (Figs. 6d'–f').

385 **4.4.2. The role of wind-driven upwelling on bay-ocean water exchange**

386 Wind-driven upwelling introduced cold water into JB contributing to water renewal.
387 For a deeper analysis of the upwelling-induced water exchange between the bay and the
388 ocean with varying wind directions and strengths, passive tracers with a concentration of 1
389 were released within each cell of the bay on the 2nd day (March 19) of simulations, when the
390 model was stable, and residence times were calculated following the methodology described
391 in Section 3.3. As bay water was exchanged with shelf water, the change rate of passive
392 tracer concentrations within JB (CR , Eq. 2) decreases exponentially whatever wind
393 conditions (Figures 7a and b). However, the decrease rate of CR , and therefore residence time
394 (RT , see tables in Fig. 7), varies depending on wind direction and strength. The flushing
395 efficiency in response to varying upwelling-favorable wind directions can be thus ranked in

396 the following order: N ($RT=5.8 d$) > NNE ($RT=7.2 d$) > NW ($RT=7.9 d$) > NE ($RT=8.1 d$) >
397 ENE ($RT=13 d$) (decreasing residence times, Figure 7a). It is concluded that when the
398 northerly wind blew over Jarvis Bay, the upwelling-induced flushing rate was highest.
399 Considering a constant wind direction (NNE), the flushing efficiency grows with increasing
400 wind strengths (residence time decreases from 25 d for no wind to 6.8 d for $0.5 N m^{-2}$, Fig.
401 7b). However, the differences on flushing efficiency become slight for wind stresses higher
402 than $0.3 N m^{-2}$ (Fig. 7b).

403 The spatial distribution of residence time (Fig. 8) demonstrates the high impact of
404 wind-driven upwelling on flushing and renovating water. The comparison of the spatial
405 distribution of bottom temperature (Fig. 5 and 6) and residence times (Fig. 8) reveals that the
406 bay regions more affected by the penetration of outer cold water in each wind scenario have
407 lower residence times and therefore higher rates of water exchange. Northeasterly winds
408 (ENE, NE and NNE) led to cool water flows to the northeastern region of the bay (Fig. 5a'-c')
409 which are characterized by much lower residence times (up to 5 days for NNE, Fig. 8.I.d)
410 than the southern-western regions (>15 days, Fig. 8.I.b-d). The closer to the north the winds
411 come, the more upstream the upwelling reaches, and the shorter the residence time in the
412 inner part. With northly winds (N), the outer cold water also flows to the western and
413 southern regions, reaching most of the bay boundary (Fig. 5.d'), and leading to a low
414 residence time in the whole bay (mean values of 6 days, Fig. 8.I.e). Residence time is lower
415 at the western and southern bay boundaries with northwesterly winds (NW, Fig. 8.I.f) in
416 relation with the direction of cold water flow. The quick renewal of water close to the
417 entrance may partly explains that the change rate (CR) for NW winds experienced a higher
418 decrease during the first days compared with NNE winds (Fig. 7a). However, the low rate of
419 renewal in the inner bay slowed this CR decrease and the residence time of the whole bay
420 was finally higher for NNE winds. This will be further discussed in Section 5.1. Considering

421 a constant wind direction (NNE), the stronger the wind, the more upstream the upwelling
422 event reaches, and the shorter the residence times. While residence times of most of the bay
423 are higher than 15 days without wind or with wind strengths of 0.05 (not shown) and 0.1 N
424 m^{-2} , water in some regions of the inner bay was renovated in 5 days for wind strengths of 0.4-
425 0.5 N m^{-2} (Fig. 8.II). Furthermore, the residence times associated to wind-driven upwelling
426 are interestingly of the same order of magnitude as those associated to atmospheric cooling
427 event during winter (7-13 days, Wang and Symonds, 1999) and to overnight cooling events
428 during summer (7-14 days, England and Moore, 2005).

429 **5. Discussion – Physical mechanism of upwelling events**

430 **5.1. Burger number**

431 In order to determine why the northerly wind had the strongest effect on the exchange
432 rate between the bay and offshore by driving deep cold water into the bay, we estimated
433 average vertical upwelling velocity ($w_c = \tau^y / \rho f R_{oi}$; τ^y is alongshore wind stress, ρ is water
434 density, f is Coriolis frequency, and R_{oi} is the internal Rossby radius of deformation) and the
435 slope Burger number ($S = \alpha N_f / f$; α is the bottom slope of the continental shelf, and $N_f =$
436 $\sqrt{gd\rho/\rho dz}$ is buoyancy frequency), which is a simple theory for the structure of two-
437 dimensional upwelling driven by wind in coastal regions (Lentz and Chapman, 2004). The
438 upwelled flow across the bay mouth from offshore can be driven by alongshore wind stress
439 (τ^y) at a scale of the internal Rossby radius of deformation. As the Burger number increases
440 (~ 1 or larger), surface wind stress or along-shelf geostrophic flow is balanced by cross-shelf
441 momentum flux divergence rather than bottom stress, and cross-shelf transport occurs
442 increasingly in the interior. While the Burger number is small ($\ll 1$), onshore flow can occur
443 dominantly in the bottom boundary layer (BBL). The area-averaged upwelling velocity (w_c)
444 and the Burger number were calculated in JB for different wind directions (Table 3). An
445 increase in mixing rate by wind stress around Jervis Bay results in a low Burger number, with

446 a reduction in N_f , making it more conducive to generate onshore flow in the BBL (Roughan
447 and Middleton, 2004; Dongxiao et al., 2012). Although Gibbs et al. (1998) showed that the
448 shift to the west of the EAC is a precondition of onshore flow triggered wind-driven
449 upwelling, we can determine the importance of two factors using the ratio of current-driven
450 upwelling flow ($v_g \delta / 2R_{oi}$) to wind-driven upwelling flow ($\tau^y / \rho f R_{oi}$). The values given to
451 the equations are $\rho = 1025 \text{ kg m}^{-3}$, $\tau^y = 0.4 \text{ N m}^{-2}$, $v_g = 0.7 \text{ m s}^{-1}$ (alongshore geostrophic
452 current), $\delta = 5 \text{ m}$ (the thickness of BBL), $R_{oi} = 7.5 \text{ km}$, and $f = 8.3 \times 10^{-5}$, yielding a ratio
453 of 0.37. We can hence show that wind-driven upwelling can be substantially more effective
454 than current-driven upwelling in inducing bottom cold water toward the entrance of JB.

455 We also analyzed the circulation within the bay in response to varying wind directions
456 with the distribution of daily depth-averaged w -velocity along with bottom temperature and
457 bottom currents (Fig. 9). When wind blew toward the coast within the bay, the water piled up,
458 causing downwelling motion. We found that this wind-driven downwelling motion in the
459 western part of JB generated by local-wind forcing within the bay played a key role in
460 blocking the intrusion of cold water upwelled through the bay entrance, as shown in Fig. 9. In
461 the shallow water system, the down-estuary wind (northwesterly) enhanced surface outflow.
462 However, the volume variation of cold water (18°C) and the residence time of the whole bay
463 was smaller than in the case of the alongshore wind (north-northeasterly) because the down-
464 estuary wind (NW) had less effect on generating surface Ekman transport in the offshore
465 direction (Fig. 5 a' and 5e'). We can hence demonstrate that the outflow of surface water
466 driven by alongshore-wind stress (such as a north-northeasterly wind in the Southern
467 Hemisphere) is replaced by bottom cold water upwelled near the coast by Ekman transport
468 (Smith, 1981). However, the volume variation of cold water in response to the northerly wind
469 was larger than in the case of the alongshore wind direction (NNE, 30°).

470 **5.2. Momentum and vorticity balances of upwelling events**

471 For further analysis of the effect of wind-driven flow within the bay in response to
 472 varying wind directions, we examined the momentum balance in the following equations:

$$473 \quad \frac{\partial u}{\partial t} + \vec{v} \cdot \nabla u + w \frac{\partial u}{\partial z} - f v = -g \frac{\partial \zeta}{\partial x} - \frac{1}{\rho} \frac{\partial P}{\partial x} + \frac{\partial}{\partial z} \left(K_m \frac{\partial u}{\partial z} \right) \quad (7)$$

$$474 \quad \frac{\partial v}{\partial t} + \vec{v} \cdot \nabla v + w \frac{\partial v}{\partial z} + f u = -g \frac{\partial \zeta}{\partial y} - \frac{1}{\rho} \frac{\partial P}{\partial y} + \frac{\partial}{\partial z} \left(K_m \frac{\partial v}{\partial z} \right) \quad (8)$$

475 where u , v , and w for velocity are x , y , and z components, respectively; ζ is surface elevation;
 476 P is baroclinic pressure; K_m is vertical viscosity (2×10^{-4}); g is gravitational acceleration; \vec{v} is
 477 the velocity vector; and t is time. We selected two points, bay entrance (M2 in Fig. 1c) and
 478 middle part (M1 in Fig. 1c) of the bay, where upwelling event is clearly identified in Figs. 5
 479 and 6. Figure 10 shows the eastward (x) and northward (y) momentum balances at sites M1
 480 and M2, and Table 4 collects the ratios between each of the terms of these momentum
 481 balance. The momentum balance within the bay without wind forcing features a linear
 482 geostrophic flow in which the surface elevation gradient (EG) is mainly balanced by the
 483 baroclinic pressure gradient (PG) and Coriolis force (FV) (not shown). At the bay entrance,
 484 EG is balanced by the horizontal advection (AH) term (not shown). Although the momentum
 485 balance with wind forcing of varying directions is still dominated by a balance between EG,
 486 FV, and PG, nonlinear ageostrophic terms such as AH, vertical advection (AV), and vertical
 487 diffusion (shear stress, KM) play a more important role (Figs. 10a and 10b and Table 4). In
 488 the eastward direction, the northerly wind (N) produced at M1 the largest FV to balance PG
 489 and KM terms ($|FV|:|PG|:|KM|=|4.0|:|3.4|:|2.4|$, Table 4). In the northward (y) direction, the
 490 largest EG term is also balanced by a relatively larger PG and KM terms
 491 ($|EG|:|PG|:|KM|=|19.1|:|9.3|:|9.8|$) in comparison with the cases of NW
 492 ($|EG|:|PG|:|KM|=|9.3|:|2.9|:|6.3|$) and NNE ($|EG|:|PG|:|KM|=|11|:|2.8|:|7.9|$) winds. The above
 493 analysis of momentum balance explains why the northerly wind (N) generated the largest
 494 upwelling intrusion into the bay.

495 Similarly, at the bay entrance, the momentum balance is dominated by EG, KM, FV,
 496 and PG terms (Table 4), although at a depth below 10 m, a complex nonlinear process played
 497 a more important role in keeping the momentum balance (Figs. 10c and 10d). Note that at the
 498 bay entrance, N and NW wind forcing generated large velocity shear in the cross-shore flow
 499 (Fig. 10d), resulting in a strong flushing rate at this region (Fig. 8.I.e-f).

500 Based on the momentum balance equation (Eqs. 7 and 8), we also estimated bay-
 501 averaged value of the vorticity balance to understand the formation mechanism of the
 502 upwelling event (Figs. 10a'-d'). The vorticity balance equation (9) is calculated as follows:

$$503 \quad \frac{\partial F}{\partial t} + u \frac{\partial F}{\partial x} + v \frac{\partial F}{\partial y} + w \frac{\partial F}{\partial z} + (F+f) \left(\frac{\partial u}{\partial x} + \frac{\partial v}{\partial y} \right) = \text{curl}(\tau^s) \quad (9)$$

504 where $F = \partial v / \partial x - \partial u / \partial y$ and τ^s is the friction term. Here the first term on the left side of Eq.
 505 9 is local time change of vorticity; the second, third, and fourth terms are advection; the fifth
 506 term is divergence or stretching.

507 We can find that in NNE and N wind forcing, advection term is mainly balanced by
 508 wind stress, in particular, on the fifth day of model run (Figs. 10a' and 10b'), but in NW,
 509 divergence term is balanced by wind stress and advection term (Fig. 10c'). As analyzed in
 510 momentum balance, the down-estuary wind (NW) led to a small volume variation of cold
 511 water because the wind direction (NW) had less effect on generating surface Ekman transport
 512 and thus coastal upwelling. It is believed that the vorticity balance without wind forcing has
 513 little effect on the circulation within the bay (Fig. 10d').

514 **6. Conclusions**

515 The Princeton Ocean Model (POM; Mellor, 2004) was adopted with a downscaling
 516 approach for a regional ocean model (JB model) nested into a global ocean model. One
 517 upwelling event in March, 2011 was detected from observed wind data and satellite SST
 518 images. The validated JB model was used to investigate the variation of the upwelling event
 519 with varying wind directions and strengths. We found that, as bottom water driven by wind

520 entered the bay, it was deflected to the south, with strong currents occurring in the center of
521 the southern basin. However, the behavior of bottom water that intruded into the bay varied
522 with different wind directions and strengths. The northerly wind (N) created the strongest
523 upwelling intrusion into the bay and the higher water renewal. Upwelling-favorable wind
524 directions for flushing efficiency can be ranked in the following order: N (0°; northerly) >
525 NNE (30°; north-northeasterly) > NW (315°; northwesterly) > NE (45°; northeasterly) > ENE
526 (60°; east-northeasterly). Northwesterly (NW) wind substantially contributed to water
527 exchange and flushing in the southern part of the bay, while other upwelling-favorable wind
528 directions had only minor effects on this region.

529 Wind-driven downwelling within the bay played a key role in blocking the intrusion
530 of the cold water upwelled through the bay entrance: in other words, the downwelling event
531 that occurred (in particular, by NNE, NE, and ENE winds in the western part of the bay)
532 could weaken the penetration of cold water into the bay. As a result, although the alongshore
533 wind direction (NNE) had a dramatic effect in generating upwelling through surface Ekman
534 transport offshore, the volume variation of cold water was larger in response to the northerly
535 wind than in response to the NNE. We also found that although the down-estuary wind (NW)
536 led to an enhanced exchange rate of total volume within the bay, the volume variation of cold
537 water was small (and therefore the residence time in the inner estuary was high) because the
538 wind direction (NW) had less effect on generating surface Ekman transport and thus coastal
539 upwelling.

540 The momentum balance inside the bay revealed that northerly wind produced the
541 largest Coriolis force to balance pressure gradient and shear stress, in comparison with cases
542 of NW and NNE winds. As a result, the northerly wind generated the largest upwelling
543 intrusion into the bay. The northerly wind hence provided the most effective forcing to bring
544 shelf cold water to the northern part of the bay. Similarly, the momentum balance at the bay

545 entrance was dominated by the Coriolis force, shear stress and surface elevation gradient
546 terms in the upper layer, although it was also controlled by a complex nonlinear process in
547 middle and lower layers. Northerly wind forcing generated a large velocity shear with
548 offshore flow at the surface and onshore flow at depth, yielding a strong flushing rate in the
549 bay.

550 **Acknowledgments**

551 The data for the project is managed by UNSW's ResData portal. The data will be made
552 available by registration with Research Data Australia (<http://researchdata.and.s.org.au/>). Any
553 users of these datasets are required to clearly acknowledge the support of UNSW and DSTO.
554 Jervis Bay bathymetry data was provided by Mr Les Hamilton, DSTO. Donghui Jiang's PhD
555 has been supported by the UNSW Canberra Defence Related Research Funding scheme and
556 the DSTO scholarship program. This work was also supported by the National Computational
557 Infrastructure National Facility at the Australian National University. We thank J. Kesby for
558 useful comments. This is publication no. 24 of the Sino-Australian Research Centre for
559 Coastal Management.

560

561

562

563

564

565

566

567

568

569

570

571

572

573

574

575

576 **References**

- 577 Abdelrhman, M. A., 2005. Simplified modeling of flushing and residence times in 42
578 embayments in New England, USA, with special attention to Greenwich Bay, Rhode
579 Island. *Estuarine, Coastal and Shelf Science*, 62, 339–351, doi:
580 10.1016/j.ecss.2004.09.021
- 581 Anderson, D. M., Burkholder, J. M., Cochlan, W. P., Glibert, P. M., Golbler, C. J., Heil, C.
582 A., Kudela, R.M., Parsons, M. L., Rensel, J. E. J., Townsend, D. W., Trainer, V. L.,
583 Vargo, G. A., 2008. Harmful algal blooms and eutrophication: Examining linkages from
584 selected coastal regions of the United States, *Harmful Algae*, 8(1), 39-53, doi:
585 10.1016/j.hal.2008.08.017.
- 586 Blackburn, S. I., Cresswell, G., 1993. A Coccolithophorid bloom in Jervis Bay, Australia,
587 *Aust. J. Mar. Freshw. Res.*, 44(2), 253-260, doi: 10.1071/MF9930253.
- 588 Brassington, G. B., Freeman, J., Huang, X., Pugh, T., Oke, P. R., Sandery, P. A., Taylor, A.,
589 Andreu-Burillo, I., Schiller, A., Griffin, D. A., Fiedler, R., Mansbridge, J., Beggs, H.,
590 Spillman, C. M., 2012. Ocean Model, Analysis and Prediction System: Version 2,
591 CAWCR Technical Report No. 052.
- 592 Brassington, G. B., Pugh, T., Spillman, C., Schulz, E., Beggs, H., Schiller, A., Oke, P. R.,
593 2007. BLUElink > Development of operational oceanography and servicing in Australia,
594 *J. Res. Prac. Inf. Tech.*, 39(2), 151-164.
- 595 Cucco, A., Umgiesser, G., Ferrarin, C., Perilli, A., Canu, D. M., Solidoro, C., 2009. Eulerian
596 and lagrangian transport time scales of a tidal active coastal basin. *Ecological Modelling*,
597 220, 913–922, doi: 10.1016/j.ecolmodel.2009.01.008
- 598 Dombrowsky, E., Bertino, L., Brassington, G., Chassignet, E., Davidson, F., Hurlburt, H.,
599 Kamachi, M., Lee, T., Martin, M., Mei, S., Tonani, M., 2009. GODAE systems in
600 operation, *Oceanogr.*, 22(3), 80-95, doi: 10.5670/oceanog.2009.68.

601 England, M., Moore, S., 2005. On the summertime buoyancy-driven circulation of Jervis Bay.
602 Marine and Freshwater Research, Peter Holloway Memorial Edition. University of New
603 South Wales, Australia.

604 García-Reyes, M., Largier, J., 2010. Observations of increased wind-driven coastal upwelling
605 off central California, *J. Geophys. Res.*, 115(C04011), doi:10.1029/2009JC005576.

606 Gibbs, M. T., Marchesiello, P., Middleton, J. H., 1997. Nutrient enrichment of Jervis Bay,
607 Australia, during the massive 1992 coccolithophorid bloom, *Mar. Freshw. Res.*, 48, 473-
608 478, doi: 10.1071/MF97035.

609 Gibbs, M. T., Middleton, J. H., Marchesiello, P., 1998. Baroclinic response of Sydney shelf
610 waters to local wind and deep ocean forcing, *J. Phys. Oceanogr.*, 28(2), 178-190, doi:
611 10.1175/1520-0485(1998)028<0178:BROSSW>2.0.CO;2.

612 Grifoll, M., Del Campo, A., Espino, M., Mader, J., González, M., & Borja, Á., 2013. Water
613 renewal and risk assessment of water pollution in semi-enclosed domains: Application
614 to Bilbao Harbour (Bay of Biscay). *Journal of Marine Systems*, 109–110, S241–S251,
615 doi: 10.1016/j.jmarsys.2011.07.010

616 Hallegraeff, G. M., Jeffery, S. W., 1993. Annually recurrent diatom blooms in spring along
617 the New South Wales coast of Australia, *Aust. J. Mar. Freshw. Res.*, 44(2), 325-334, doi:
618 10.1071/MF9930325.

619 Herzfeld, M., Tomczak, M., 1999. Bottom-driven upwelling generated by eastern
620 intensification in closed and semi-closed basins with a slope bottom, *Mar. Freshw. Res.*,
621 50(7), 613-627, doi: 10.1071/MF98035.

622 Holloway, P. E., Symonds, G., Nunes Vaz, R., 1992a. Acoustic Doppler Current Profiler
623 measurements in Jervis Bay, December 1990 to January 1991 and July 1991 to
624 September 1991. Working paper 1992/2. Department of Geography and Oceanography,
625 University College, Australian Defence Force Academy, 13 pp.

626 Holloway, P. E., Symonds, G., Nunes Vaz, R., 1992b. Observations of circulation and
627 exchange processes in Jervis Bay, New South Wales, *Aust. J. Mar. Freshw. Res.*, 43,
628 1487-1515, doi: 10.1071/MF9921487.

629 Holloway, P. E., Symonds, G., Nunes Vaz, R., Jeffrey, M., 1991. Oceanographic
630 measurements in Jervis Bay: April 1989 to April 1990. In Working paper 1991/1,
631 Department of Geography and Oceanography, University College, Canberra, ACT,
632 Australian Defence Force Academy, The University of New South Wales.

633 Hu, J. Y., Kawamura, H., Hong, H. S., Suetsugu, M., Lin, M. S., 2001. Hydrographic and
634 satellite observations of summertime upwelling in the Taiwan strait, a preliminary
635 description, *Terr. Atmos. Ocean. Sci.*, 12(2), 415-430.

636 Huyer, A., Smith, R. L., Stabeno, P. J., Church, J. A., White, N. J., 1988. Currents off South-
637 eastern Australia: Results from the Australian coastal experiment, *Aust. J. Mar. Freshw.*
638 *Res.*, 39(3), 245-88, doi: 10.1071/MF9880245.

639 Joyce, A., Rubio-Zuazo, A. M., Winberg, P. C., 2010. Environmental and Socio-Economic
640 Considerations for Aquaculture in Jervis Bay, NSW, Canberra: Fisheries Research and
641 Development Corporation.

642 Kai, M., Hara, T., Aoyama, H., Kuroda, N., 1999. A massive Coccolithophorid bloom
643 observed in Mikawa Bay, Japan, *J. Oceanogr.*, 55(3), 395-406, doi:
644 10.1023/A:1007806500053.

645 Krishnamurti, T. N., Rajendran, K., Vijaya Kumar, T. S. V., Lord, S., Toth, Z., Zou, X.,
646 Cocks, S., Ahlquist, J. E., Navon, I. M., 2003. Improved skill for the anomaly
647 correlation of geopotential heights at 500 hPa, *Mon. Weather Rev.*, 131(6), 1082-1102,
648 doi: 10.1175/1520-0493(2003)131<1082:ISFTAC>2.0.CO;2.

649 Lee, R. S., Pritchard, T. R., Ajani, P. A., Black, K. P., 2007. The influence of the East
650 Australian Current eddy field on phytoplankton dynamics in the coastal zone, *J. Coast.*
651 *Res.*, 50, 576-584.

652 Lentz, S. J., Chapman, D. C., 2004. The importance of nonlinear cross-shelf momentum flux
653 during wind-driven coastal upwelling, *J. Phys. Oceanogr.*, 34, 2444-2457,
654 doi:10.1175/JPO2644.1.

655 Lewis, R. K., 1981. Seasonal upwelling along the South-eastern coastline of South Australia,
656 *Aust. J. Mar. Freshw. Res.*, 32(6), 843-854, doi: 10.1071/MF9810843.

657 Liu, Z., Wei, H., Liu, G., & Zhang, J., 2004. Simulation of water exchange in Jiaozhou Bay
658 by average residence time approach. *Estuarine, Coastal and Shelf Science*, 61(1), 25–35,
659 doi: 10.1016/j.ecss.2004.04.009

660 Marcello, J., Marques, F., Eugenio, F., 2005. Automatic tool for the precise detection of
661 upwelling and filaments in remote sensing imagery, *IEEE Trans. Geosci. Remote Sens.*,
662 43(7), 1605-1616, doi: 10.1109/TGRS.2005.848409.

663 Marchesiello, P., Middleton, J., 2000. Modelling the East Australian Current in the Western
664 Tasman Sea, *J. Phys. Oceanogr.*, 30(11), 2956-2971, 10.1175/1520-
665 0485(2001)031<2956:MTEACI>2.0.CO;2.

666 Masson, D., and P. Cummins (2004), Observations and modelling of seasonal variability in
667 the Straits of Georgia and Juan de Fuca, *J. Mar. Res.*, 62(4), 491-516, doi:
668 10.1357/0022240041850075.

669 Matsumoto, K., Takanezawa, T., Ooe, M., 2000. Ocean tide models developed by
670 assimilating TOPEX/POSEIDON altimeter data into hydrodynamical model: A global
671 model and a regional model around Japan, *J. Oceanogr.*, 56(5), 567-581, doi:
672 10.1023/A:1011157212596.

673 McClean-Padman, J., Padman, L., 1991. Summer upwelling on the Sydney inner continental
674 shelf: the relative roles of local wind forcing and mesoscale eddy encroachment, *Cont.*
675 *Shelf Res.*, 11(4), 321-345, doi: 10.1016/0278-4343(91)90025-2.

676 Mellor, G. L., 2004. Users Guide for A Three-dimensional, Primitive Equation, Numerical
677 Ocean Model, Princeton University, Princeton, NJ.

678 Mellor, G. L., Yamada, T., 1982. Development of a turbulence closure model for geophysical
679 fluid problems, *Rev. Geophys. Space Phys.*, 20(4), 851-875, doi:
680 10.1029/RG020i004p00851.

681 Middleton, J. F., 1994. The baroclinic response of straits and bays to coastal-trapped wave
682 scattering, *J. Phys. Oceanogr.*, 24(3), 521-539, doi: 10.1175/1520-
683 0485(1994)024<0521:TBROSA>2.0.CO;2.

684 Oddo, P., Pinardi, N., 2008. Lateral open boundary conditions for nested limited area models:
685 A scale selective approach, *Ocean Model.*, 20(2), 134-156, doi:
686 10.1016/j.ocemod.2007.08.001.

687 Oke, P. R., Brassington, G. B., Griffin, D. A., Schille, A., 2008. The Bluelink Ocean Data
688 Assimilation System (BODAS), *Ocean Model.*, 21(1-2), 46-70, doi:
689 10.1016/j.ocemod.2007.11.002.

690 Oke, P. R., Middleton, J. H., 2001. Nutrient enrichment off Port Stephens: The role of the
691 East Australian Current, *Cont. Shelf Res.*, 21(6-7), 587-606, doi: 10.1016/S0278-
692 4343(00)00127-8.

693 Oke, P. R., Sakov, P., Cahill, M. L., Dunn, J. R., Fiedler, R., Griffin, D. A., Mansbridge, J. V.,
694 Ridgway, K. R., Schiller, A., 2013. Towards a dynamically balanced eddy-resolving
695 ocean reanalysis: BRAN3, *Ocean Model.*, 67, 52-70, doi:
696 10.1016/j.ocemod.2013.03.008.

697 Perkins, A. L., Smedstad, L. F., 1998. Scale-related aspects of nested finite difference ocean
698 models, *Theor. Comput. Fluid Dynam.*, 10(1-4), 311-322, doi: 10.1007/s001620050066.

699 Pond, S., Pickard, G. L., 1983. *Introductory Dynamical Oceanography*, 2nd ed., 329 pp.,
700 Pergamon Press, Oxford, UK.

701 Pritchard, T. R., Lee, R. S., Ajani, P. A., Rendell, P. S., Black, K., Koop, K., 2003.
702 Phytoplankton responses to nutrient sources in coastal waters off Southeastern Australia,
703 *Aquat. Ecosys. Health Manag.*, 6(2), 105-117, doi: 10.1080/14634980390199806.

704 Rochford, D. J., 1984. Nitrates in eastern Australian coastal waters, *Aust. J. Mar. Freshw.*
705 *Res.*, 35(4), 385-397, doi: 10.1071/MF9840385.

706 Roughan, M., Middleton, J. H., 2004. On the East Australian Current: Variability,
707 encroachment, and upwelling, *J. Geophys. Res.*, 109, C07003,
708 doi:10.1029/2003JC001833.

709 Schahinger, R. B., 1987. Structure of coastal upwelling events observed off the South-east
710 coast of South Australia during February 1983-April 1984, *Aust. J. Mar. Freshw. Res.*,
711 38(4), 439-459, doi: 10.1071/MF9870439.

712 Schiller, A., Oke, P. R., Brassington, G., Entel, M., Fiedler, R., Griffin, D. A., Mansbridge, J.
713 V., Meyers, G. A., Ridgway, K. R., Smith, N. R., 2008. Eddy-resolving ocean
714 circulation in the Asian-Australian Region inferred from an ocean reanalysis effort, *Prog.*
715 *Oceanogr.*, 76(3), 334-365, doi: 10.1016/j.pocean.2008.01.003.

716 Smith, R. L., 1968. Upwelling, *Oceanography and Marine Biology Annual Reviews*, 6, 11-46.

717 Smith, R. L., 1981. A comparison of the structure and variability of the flow field in three
718 coastal upwelling regions: Oregon, northwest Africa, and Peru, in *Coastal Upwelling*,
719 *Coastal Estuarine Sci. Ser.*, vol. 1, edited by F. A. Richards, pp. 107-118, AGU,
720 Washington, D.C.

721 Sommerfeld, A., 1949. *Partial Differential Equations in Physics*. Academic Press, 355 pp.

722 Thomas, M. D., 1998, Jervis Bay: Winter circulation characteristics, BSc Thesis, School of
723 Geography and Oceanography University College, Australian Defence Force Academy,
724 UNSW.

725 Trainer, V. L., Adams, N. G., Bill, B. D., Stehr, C. M., Wekell, J. C., Moeller, P., Busman,
726 M., Woodruff, D., 2000. Domoic acid production near California coastal upwelling
727 zones, June (1998), *Limnol. Oceanogr.*, 45(8), 1818-1833.

728 Tranter, D. J., Carpenter, D. J., Leech, G. S., 1986. The coastal enrichment effect of the East
729 Australian Current eddy field, *Deep Sea Res.*, 33(11-12), 1705-1728.

730 Trenbreth, K. E., Large, W. G., Olsen, J. G., 1990. The mean annual cycle in global ocean
731 wind stress, *J. Phys. Oceanogr.*, 20(11), 1742-1760, doi: 10.1175/1520-
732 0485(1990)020<1742:TMACIG>2.0.CO;2.

733 Wang, X. H., Symonds, G., 1999. Coastal embayment circulation due to atmospheric cooling,
734 *J. Geophys. Res.*, 104(12), 29,801-29,816.

735 Wang, X. H., Wang, X. L., 2003. A numerical study of water circulation in a thermally
736 stratified embayment, *J. Ocean Univ. China*, 2(1), 24-34, doi: 10.1007/s11802-003-
737 0022-3.

738 Wang, X. H., Bhatt, V., Sun, Y.-J., 2013. Study of seasonal variability and heat budget of the
739 East Australian Current using two eddy-resolving ocean circulation models, *Ocean*
740 *Dynam.*, 63(5), 549-563, doi: 10.1007/s10236-013-0605-5.

741 Wang, X. H., Bhatt, V., Sun, Y.-J., 2015. Seasonal and inter-annual variability of western
742 subtropical mode water in the South Pacific Ocean, *Ocean Dynam.*, 65(1), 143-154, doi:
743 10.1007/s10236-014-0792-8.

744 Yamamoto, T., 2003. The Seto Inland Sea-eutrophic or oligotrophic?, *Marine Pollut. Bull.*,
745 47(1-6), 37-42, doi: 10.1016/S0025-326X(02)00416-2.

746

747 LIST OF TABLES

748 **Table 1.** Absolute and relative differences between observation and model results for each
749 tidal constituent used to force the model for the year 1998.

750 **Table 2.** Cases for numerical experiments of an upwelling event.

751 **Table 3.** Area-averaged upwelling velocity (w_c , 10^{-4} m s $^{-1}$) and Burger number (S) within the
752 bay varying with different wind directions.

753 **Table 4.** Relative contribution of each of the terms of the momentum equations represented
754 in Figure 10, which were determined in the eastward (x) and northward (y) directions on
755 March 21, 2011 at sites M1 and M2 (Fig. 1c). Ratios were calculated by averaging in depth
756 the absolute values of each term. Linear terms are: FV, Coriolis force; EG, surface elevation
757 gradient; and PG, baroclinic pressure gradient. Non-linear terms were underlined to facilitate
758 comparisons: AH, horizontal advection; AW, vertical advection; KM, vertical diffusion; and
759 AT, acceleration.

760

761

762

763

764

765

766

767

768

769

770

771

772

773

774

775

776 **Table 1.** Absolute and relative differences between observation and model results for each
777 tidal constituent used to force the model for the year 1998.

Tidal components		O ₁	K ₁	M ₂	S ₂
1998	Absolute error, <i>D</i> (cm)	0.8	5.1	3.4	4.9
	Absolute phase error (°)	2.0	0.5	0.4	1.6

778

779 **Table 2.** Cases for numerical experiments of an upwelling event.

Case	Direction	Strength (N m ⁻²)	Case	Strength (constant wind direction of NNE)	
				Wind stress	Wind speed
				(N m ⁻²)	(m s ⁻¹)
			S1	0.0 (no-wind)	
D1	NNE (30°)	0.4	S2	0.05	6.0
D2	ENE (60°)		S3	0.1	8.5
D3	NE (45 °)		S4	0.2	11.5
D4	N (0 °)		S5	0.3	13.4
D5	NW (315°)		S6	0.4	15.0
			S7	0.5	16.3

780

781 **Table 3.** Area-averaged upwelling velocity (w_c , 10^{-4} m s $^{-1}$) and Burger number (S) within the
 782 bay varying with different wind directions.

	NNE (30°)	N (0°)	NW (315°)	NE (45°)	ENE (60°)	No wind
w_c	5.37	6.04	4.46	4.24	2.73	0
S	0.861	0.853	0.874	0.888	0.928	1.035

783

784 **Table 4.** Relative contribution of each of the terms of the momentum equations represented
785 in Figure 10, which were determined in the eastward (x) and northward (y) directions on
786 March 21, 2011 at sites M1 and M2 (Fig. 1c). Ratios were calculated by averaging in depth
787 the absolute values of each term. Linear terms are: FV, Coriolis force; EG, surface elevation
788 gradient; and PG, baroclinic pressure gradient. Non-linear terms were underlined to facilitate
789 comparisons: AH, horizontal advection; AW, vertical advection; KM, vertical diffusion; and
790 AT, acceleration.

791

Site/Direction	FV	EG	PG	<u> AH </u>	<u> AW </u>	<u> KM </u>	AT
N							
M1 _x	4.0	1.0	3.4	<u>0.7</u>	<u>0.2</u>	<u>2.4</u>	0.2
M1 _y	1.9	19.1	9.3	<u>3.4</u>	<u>2.7</u>	<u>9.8</u>	0.3
M2 _x	3.5	10.9	8.9	<u>6.6</u>	<u>4.2</u>	<u>2.7</u>	0.4
M2 _y	4.3	18.6	10.6	<u>5.7</u>	<u>2.3</u>	<u>6.3</u>	0.4
NW							
M1 _x	2.5	5.8	2.4	<u>0.7</u>	<u>0.5</u>	<u>6.6</u>	0.2
M1 _y	2.8	9.3	2.9	<u>1.8</u>	<u>0.8</u>	<u>6.5</u>	0.2
M2 _x	3.4	6.7	6.6	<u>8.0</u>	<u>2.8</u>	<u>4.4</u>	0.2
M2 _y	4.5	0.1	2.5	<u>5.1</u>	<u>2.3</u>	<u>4.8</u>	0.3
NNE							
M1 _x	3.4	5.8	1.9	<u>1.0</u>	<u>0.3</u>	<u>4.9</u>	0.3
M1 _y	1.6	11.0	2.8	<u>1.7</u>	<u>1.6</u>	<u>7.9</u>	0.3
M2 _x	2.7	15.6	10.5	<u>4.2</u>	<u>3.6</u>	<u>5.0</u>	0.4
M2 _y	3.1	13.6	8.5	<u>2.5</u>	<u>2.3</u>	<u>5.8</u>	0.5

792

793 LIST OF FIGURES

794 **Fig. 1.** Map of the study area: (a) schematic view of ocean circulation and fronts of the
795 Southwest Pacific Ocean region along the coastline of Australia, (b) the model domain with
796 bottom topography, and (c) a topographic map of the area around Jervis Bay in m. The
797 contour interval is 5 m. The three open circles (T1, T2, and T3) indicate the stations where
798 thermistors were moored from March to August 2011. Solid black circles indicate the
799 location of sites M1 and M2 referred to in Fig. 8. Superimposed are ADCP tracks (a–e) and
800 CTD stations (+) for June 26, 1998. Open diamonds with black crosses are stations for
801 vertical section of temperature from Callala to Bowen Island in Figs. 3g and 3g'.

802 **Fig. 2.** Images of SST on (a) March 18, 2011 and (b) March 21, 2011 with $1/12^\circ$ resolution
803 provided by RAMSSA. The red ellipses represent cold water outcropping along the coast of
804 Jervis Bay. Wind vectors for comparison of three-hourly observations (m s^{-1}) (c) and model
805 forcing data (N m^{-2}) (d) at Jervis Bay for the period from March 18–26, 2011. Observation
806 data are taken from Pt. Perpendicular AWS (see Fig. 1c) and model forcing data are extracted
807 from OceanMAPS. The black ellipses represent the period (from March 20–22, 2011) when it
808 is possible for a coastal upwelling event to occur.

809 **Fig. 3.** Comparison of current velocity for surface (a) and bottom (b) from the observation
810 data between 08–14 h on June 26, 1998 and for surface (c) and bottom (d) from daily-
811 averaged model results on June 26, 1998. Horizontal distributions of water temperature for
812 comparison of observation data between 08–14 h (e and f) and daily-averaged model results
813 on June 26, 1998 (e' and f'). The plus signs in the panels of (e and f) indicate CTD stations.
814 Vertical sections of temperature from Callala to Bowen Island (see open diamonds with
815 crosses in Fig. 1c) and from Bowen Island to Dart Point (see e-line in Fig. 1c) for observation
816 data between 08–14 h (g and h) and daily-averaged model results on June 26 1998 (g' and h').
817 The contour interval is 0.1°C .

818 **Fig. 4.** The horizontal distribution of daily-averaged surface (a-d) and bottom (a'-d')
819 temperature during the period from March 20–24, 2011. The contour interval is 1.0°C. The
820 bold solid lines of (a-d) and (a'-d') indicate the 22°C and 18°C isotherms, respectively.
821 Vectors in panels show daily-averaged surface and bottom velocities (in m s^{-1}). Superimposed
822 is the daily-averaged wind vector, with the radius of the circle indicating 0.1 N m^{-2} . Time
823 series of surface (e) and bottom (f) temperatures for comparison of model results and
824 observation data. The black solid and grey dashed lines represent observation data and model
825 results, respectively. T1, T2, and T3 indicate the stations where thermistors were moored
826 from March–August 2011 (see Fig. 1c).

827 **Fig. 5.** The distributions of daily-averaged surface (left panels) and bottom (right panels)
828 temperatures simulated with varying wind directions and a uniform wind of 0.4 N m^{-2} : (a, a')
829 NNE (30°), (b, b') ENE (60°), (c, c') NE (45°), (d, d') N (0°), and (e, e') NW (315°) in the bay
830 area on March 21, 2011. The degree of the parentheses indicates the clockwise direction from
831 the north and represents the wind blowing from that direction. The bold solid lines of (left
832 panels) and (right panels) indicate 21°C and 18°C isotherms, respectively. Vectors in each
833 panel show daily-averaged surface and bottom velocities (in m s^{-1}).

834 **Fig. 6.** The distributions of daily-averaged surface (left panels) and bottom (right panels)
835 temperature simulated with varying wind strengths and a constant upwelling-favorable wind
836 direction of NNE (30°): (a, a') without wind, (b, b') 0.1 N m^{-2} , (c, c') 0.2 N m^{-2} , (d, d') 0.3 N
837 m^{-2} , (e, e') 0.4 N m^{-2} , and (f, f') 0.5 N m^{-2} in the bay area on 21 March, 2011. The bold solid
838 lines of (left panels) and (right panels) indicate 21°C and 18°C isotherms, respectively.
839 Vectors in each panel show daily-averaged surface and bottom velocities (in m s^{-1}).

840 **Fig. 7.** Change rate of passive tracer concentration within total volume ($1.9 \times 10^9 \text{ m}^3$) of
841 Jarvis Bay (CR, Eq. 2) varying with upwelling-favorable wind direction (a) and strength (b).
842 Residence time (RT, days), computed as time required for the change rate to decrease below

843 1/e (light gray dotted lines), is detailed for each wind scenario in right Tables. Asterisks
844 indicate that the residence time was calculated from the interpolation of change rate over a
845 longer time period. The exponential functions used to fit the change rate curves for “no wind”
846 and “0.05 N m⁻²” are $CR = 0.9638e^{-0.0015time}$ ($R^2=0.986$) and $CR = 0.9701e^{-0.0019time}$
847 ($R^2=0.987$), respectively.

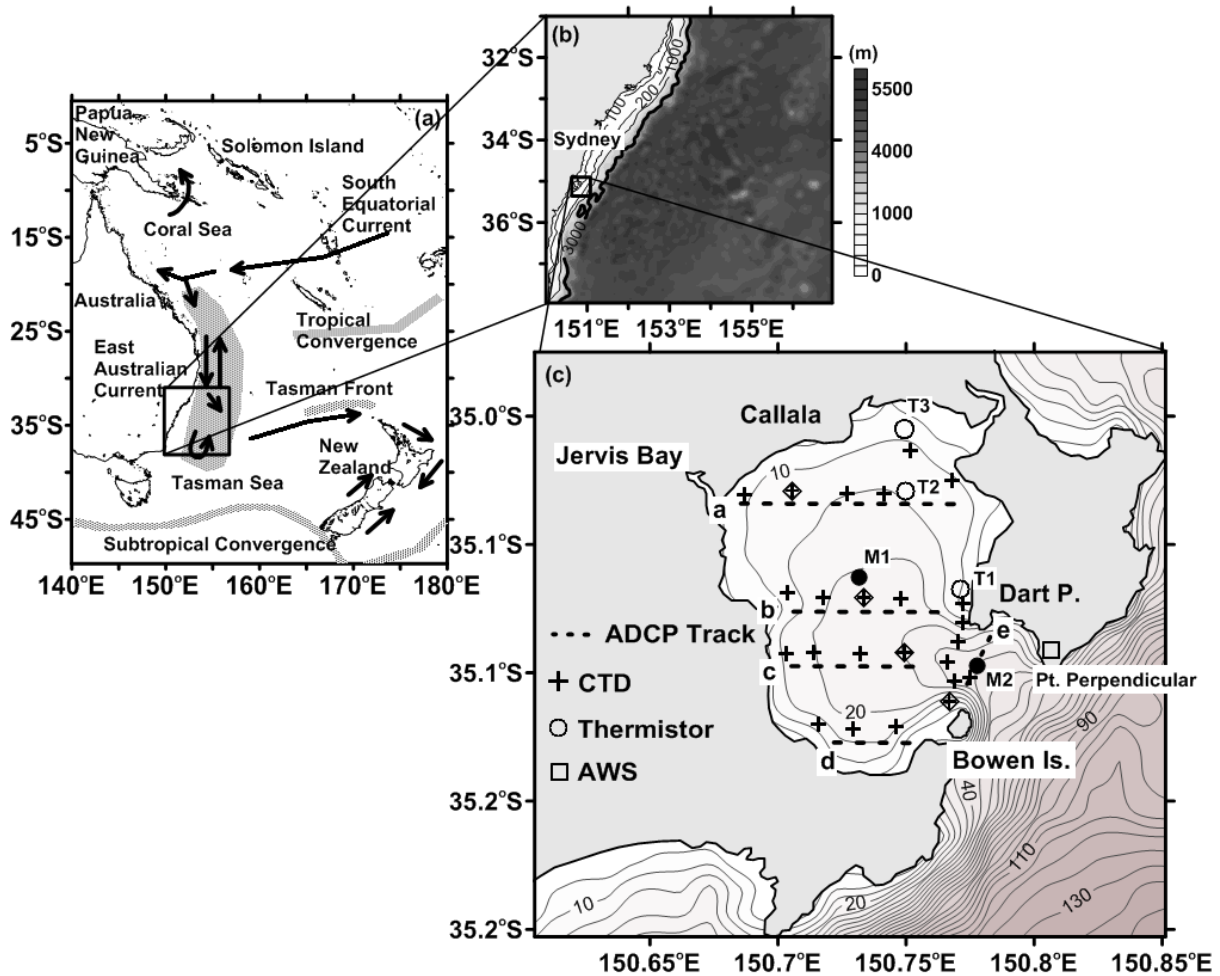
848 **Fig. 8.** (I) Spatial distribution of residence time with varying upwelling-favorable wind
849 directions and a uniform wind of 0.4 N m⁻²: (a) without wind, (b') ENE (60°), (c) NE (45°),
850 (d) NNE (30°), (e) N (0°), and (f) NW (315°). (II) Spatial distribution of residence time with
851 varying wind strengths and a constant upwelling-favorable wind direction of NNE (30°): (a,
852 a') without wind, (b) 0.1 N m⁻², (c) 0.2 N m⁻², (d) 0.3 N m⁻², (e) 0.4 N m⁻², and (f) 0.5 N m⁻².
853 2. Values higher than 15 days could not be detailed due to computation time-limits.

854

855 **Fig. 9.** The distribution of sea level, current, and temperature on March 21, 2011 for different
856 wind directions. The color shading represents daily depth-averaged w-velocity. The negative
857 sign means downward flow. Grey contour lines with 1.0°C intervals represent bottom
858 temperature. Arrow vectors are bottom current velocity (unit: m s⁻¹). Black bold dashed lines
859 with 0.01 m intervals denote daily-averaged sea levels. Superimposed is the wind vector with
860 the radius of the circle indicating 0.4 N m⁻².

861 **Fig. 10.** Vertical profiles of daily-averaged terms of momentum equations in the eastward (a,
862 c) and northward (b, d) directions on March 21, 2011 at sites M1 (a, b) and M2 (c, d) (see Fig.
863 1c), for N (0°), NW (315°), and NNE (30°). Subscripts, x and y, in M1 and M2 indicate the
864 momentum balance in the eastward and northward directions. Line colors represent the
865 following: FV, Coriolis force; EG, surface elevation gradient; PG, baroclinic pressure
866 gradient; AH, horizontal advection; AW, vertical advection; KM, vertical diffusion; and AT,

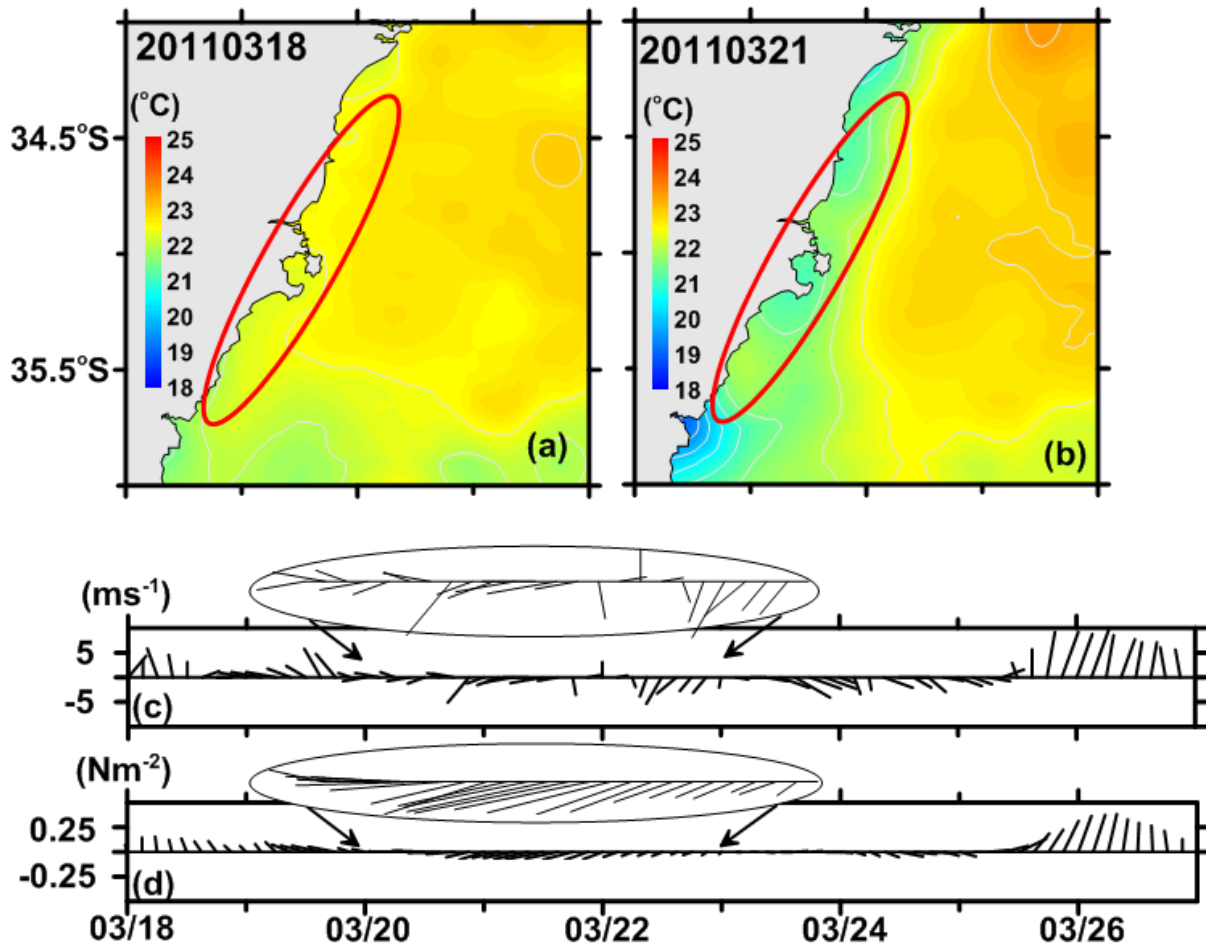
867 acceleration. Vorticity balance ($a'-d'$) of horizontally and vertically averaged circulation for
868 NNE, N, NW and no wind forcing inside the bay.



872

873 **Fig. 1.** Map of the study area: (a) schematic view of ocean circulation and fronts of the
 874 Southwest Pacific Ocean region along the coastline of Australia, (b) the model domain with
 875 bottom topography, and (c) a topographic map of the area around Jervis Bay in m. The
 876 contour interval is 5 m. The three open circles (T1, T2, and T3) indicate the stations where
 877 thermistors were moored from March to August 2011. Solid black circles indicate the
 878 location of sites M1 and M2 referred to in Fig. 8. Superimposed are ADCP tracks (a–e) and
 879 CTD stations (+) for June 26, 1998. Open diamonds with black crosses are stations for
 880 vertical section of temperature from Callala to Bowen Island in Figs. 3g and 3g'.
 881

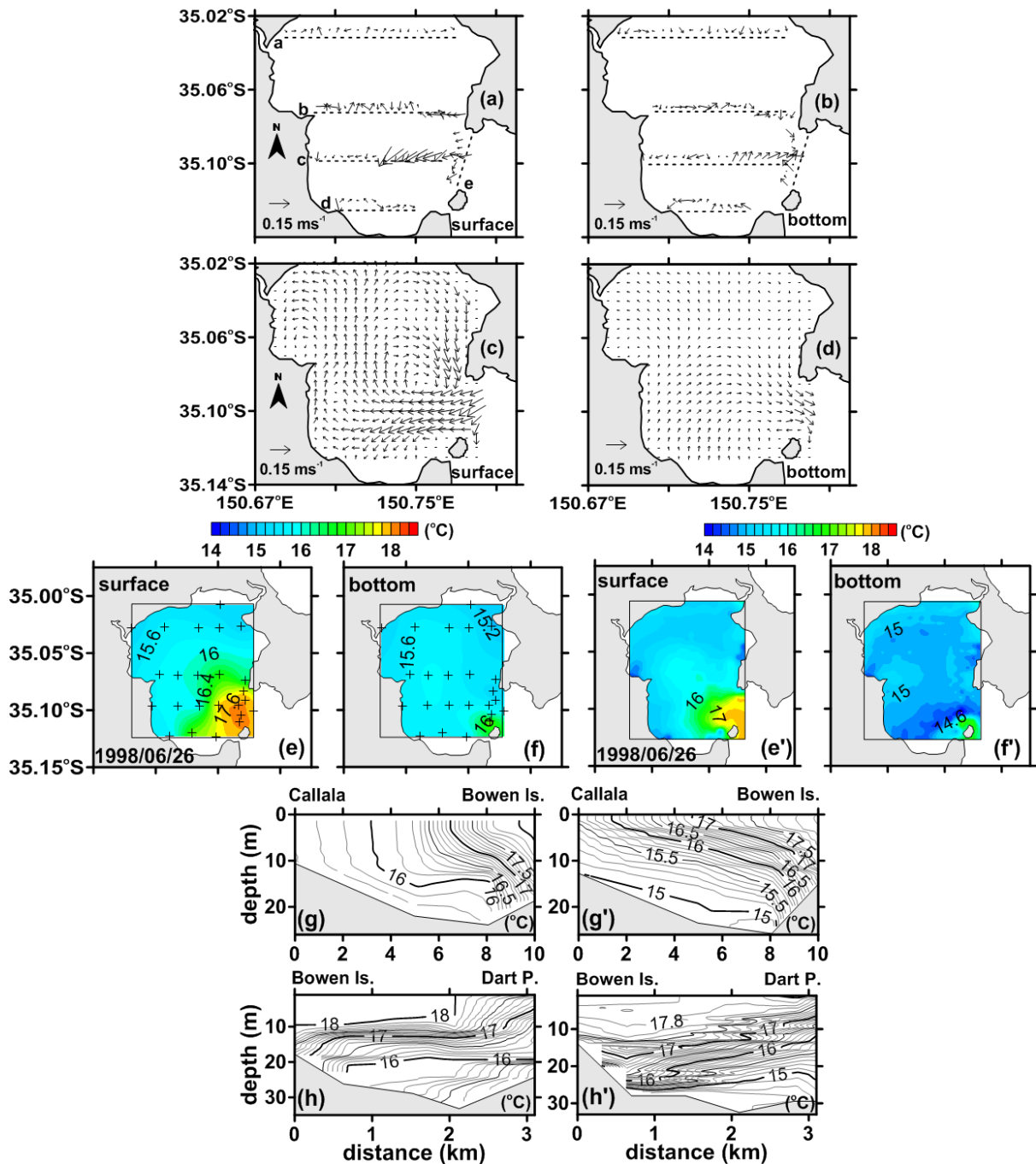
882



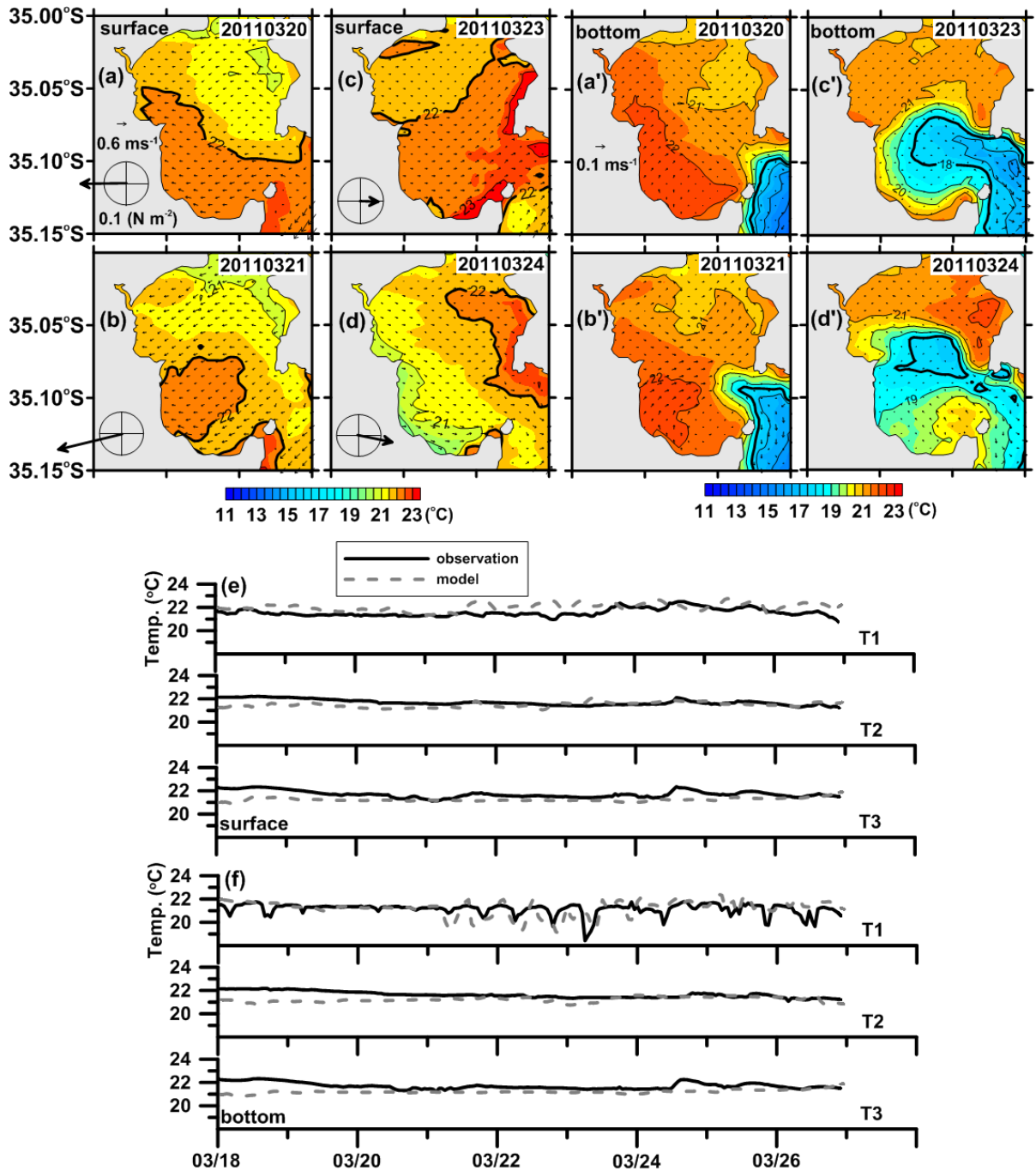
884

885 **Fig. 2.** Images of SST on (a) March 18, 2011 and (b) March 21, 2011 with $1/12^\circ$ resolution
 886 provided by RAMSSA. The red ellipses represent cold water outcropping along the coast of
 887 Jervis Bay. Wind vectors for comparison of three-hourly observations (m s^{-1}) (c) and model
 888 forcing data (N m^{-2}) (d) at Jervis Bay for the period from March 18–26, 2011. Observation
 889 data are taken from Pt. Perpendicular AWS (see Fig. 1c) and model forcing data are extracted
 890 from OceanMAPS. The black ellipses represent the period (from March 20–22, 2011) when it
 891 is possible for a coastal upwelling event to occur.

892



895 **Fig. 3.** Comparison of current velocity for surface (a) and bottom (b) from the observation
 896 data between 08–14 h on June 26, 1998 and for surface (c) and bottom (d) from daily-
 897 averaged model results on June 26, 1998. Horizontal distributions of water temperature for
 898 comparison of observation data between 08–14 h (e and f) and daily-averaged model results
 899 on June 26, 1998 (e' and f'). The plus signs in the panels of (e and f) indicate CTD stations.
 900 Vertical sections of temperature from Callala to Bowen Island (see open diamonds with
 901 crosses in Fig. 1c) and from Bowen Island to Dart Point (see e-line in Fig. 1c) for observation
 902 data between 08–14 h (g and h) and daily-averaged model results on June 26 1998 (g' and h').
 903 The contour interval is 0.1°C.



906 **Fig. 4.** The horizontal distribution of daily-averaged surface (a-d) and bottom (a'-d')

907 temperature during the period from March 20–24, 2011. The contour interval is 1.0°C. The

908 bold solid lines of (a-d) and (a'-d') indicate the 22°C and 18°C isotherms, respectively.

909 Vectors in panels show daily-averaged surface and bottom velocities (in m s⁻¹). Superimposed

910 is the daily-averaged wind vector, with the radius of the circle indicating 0.1 N m⁻². Time

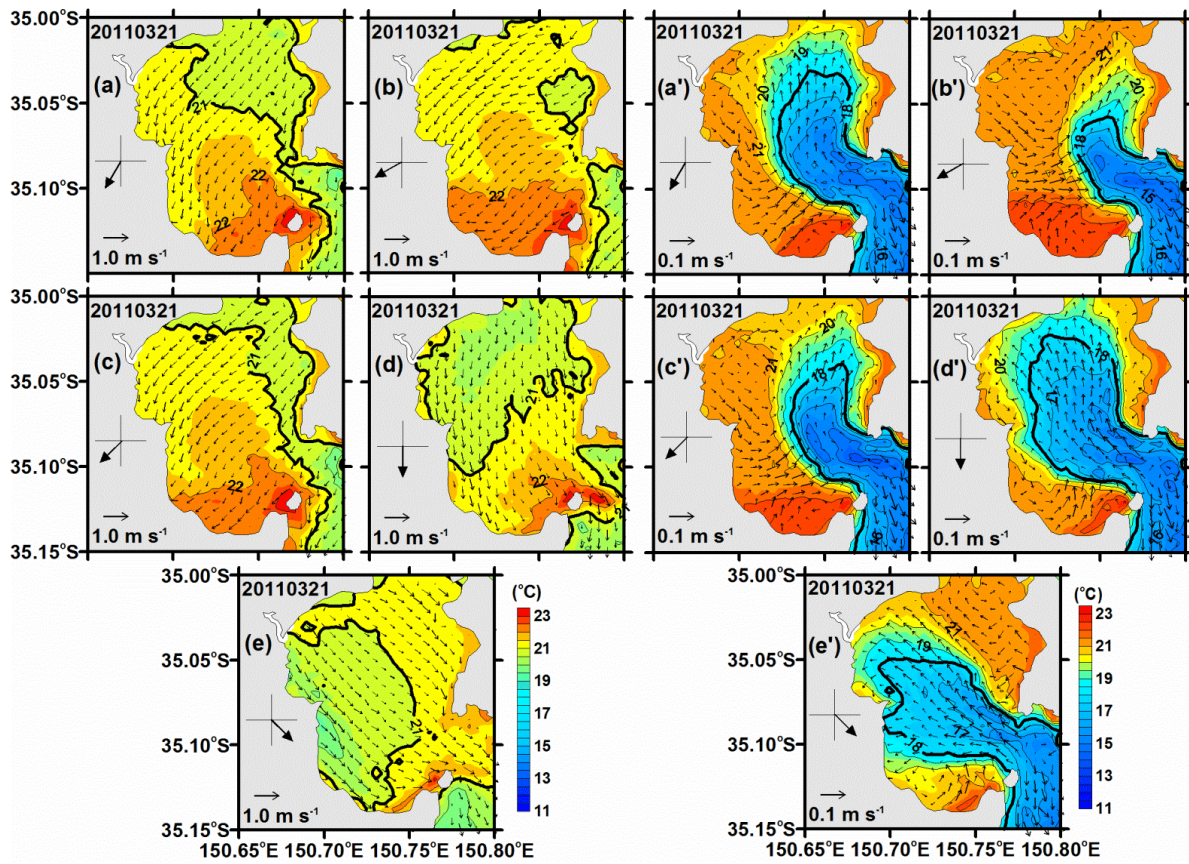
911 series of surface (e) and bottom (f) temperatures for comparison of model results and

912 observation data. The black solid and grey dashed lines represent observation data and model

913 results, respectively. T1, T2, and T3 indicate the stations where thermistors were moored

914 from March–August 2011 (see Fig. 1c).

915



916

917 **Fig. 5.** The distributions of daily-averaged surface (left panels) and bottom (right panels)
918 temperatures simulated with varying wind directions and a uniform wind of 0.4 N m^{-2} : (a, a')
919 NNE (30°), (b, b') ENE (60°), (c, c') NE (45°), (d, d') N (0°), and (e, e') NW (315°) in the bay
920 area on March 21, 2011. The degree of the parentheses indicates the clockwise direction from
921 the north and represents the wind blowing from that direction. The bold solid lines of (left
922 panels) and (right panels) indicate 21°C and 18°C isotherms, respectively. Vectors in each
923 panel show daily-averaged surface and bottom velocities (in m s^{-1}).
924

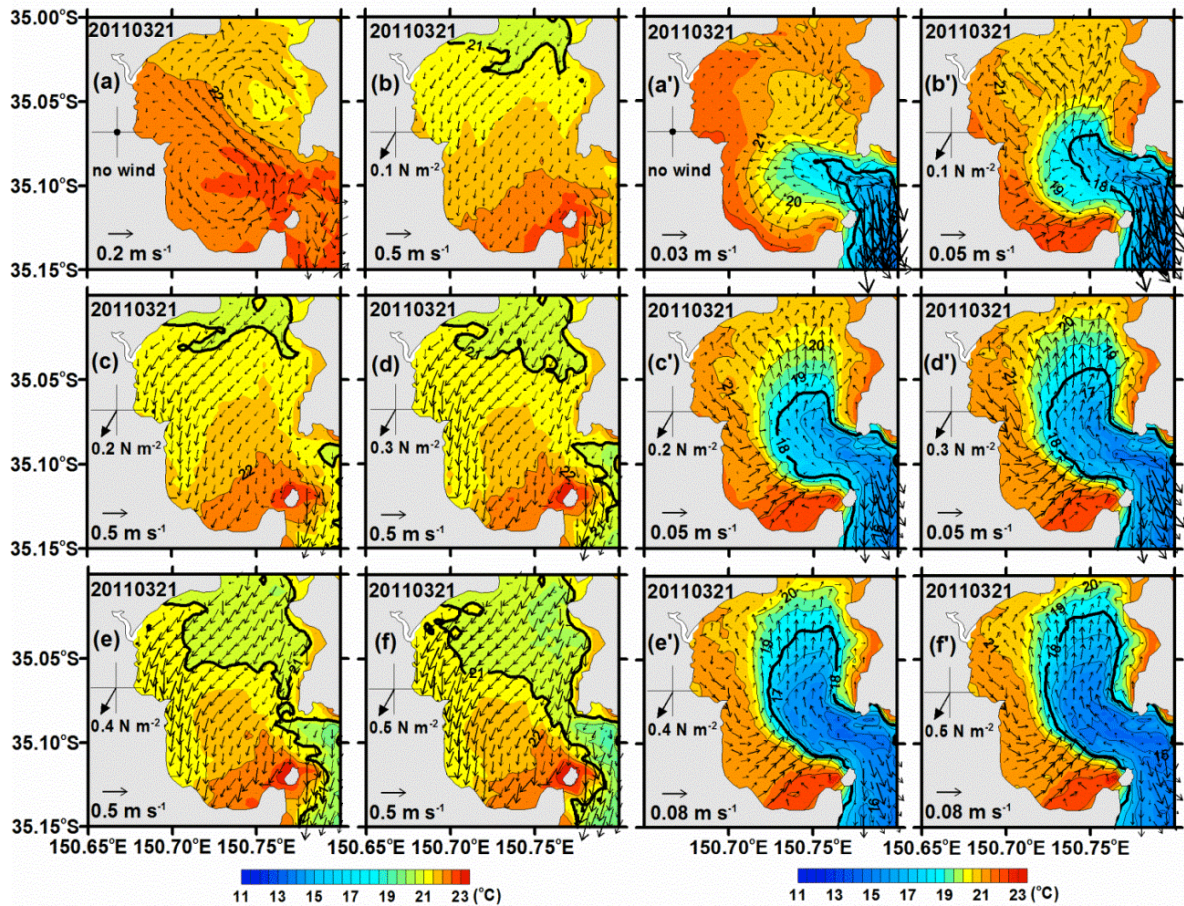
925

926

927

928

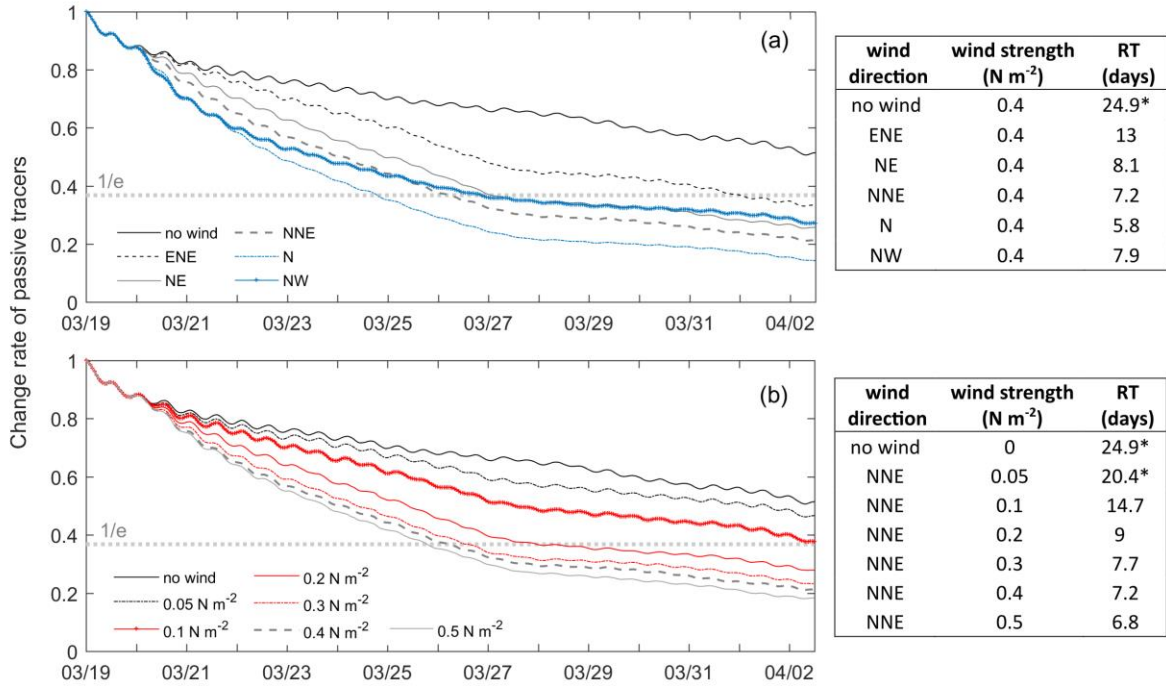
929



931

932 **Fig. 6.** The distributions of daily-averaged surface (left panels) and bottom (right panels)
 933 temperature simulated with varying wind strengths and a constant upwelling-favorable wind
 934 direction of NNE (30°): (a, a') without wind, (b, b') 0.1 N m^{-2} , (c, c') 0.2 N m^{-2} , (d, d') 0.3 N
 935 m^{-2} , (e, e') 0.4 N m^{-2} , and (f, f') 0.5 N m^{-2} in the bay area on 21 March, 2011. The bold solid
 936 lines of (left panels) and (right panels) indicate 21°C and 18°C isotherms, respectively.
 937 Vectors in each panel show daily-averaged surface and bottom velocities (in m s^{-1}).

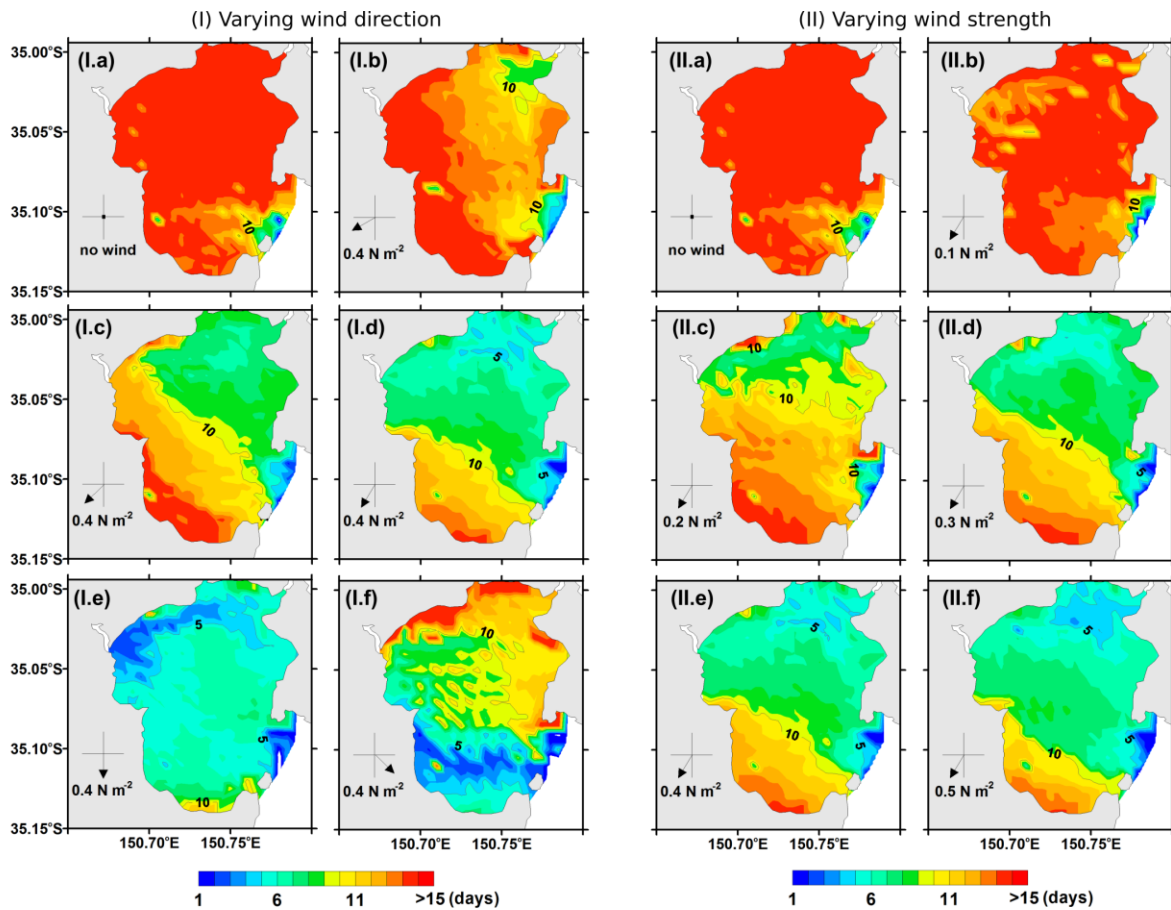
938



939

940 **Fig. 7.** Change rate of passive tracer concentration within total volume ($1.9 \times 10^9 \text{ m}^3$) of
 941 Jarvis Bay (CR, Eq. 2) varying with upwelling-favorable wind direction (a) and strength (b).
 942 Residence time (RT, days), computed as time required for the change rate to decrease below
 943 $1/e$ (light gray dotted lines), is detailed for each wind scenario in right Tables. Asterisks
 944 indicate that the residence time was calculated from the interpolation of change rate over a
 945 longer time period. The exponential functions used to fit the change rate curves for “no wind”
 946 and “ 0.05 N m^{-2} ” are $CR = 0.9638e^{-0.0015time}$ ($R^2=0.986$) and $CR = 0.9701e^{-0.0019time}$
 947 ($R^2=0.987$), respectively.

948

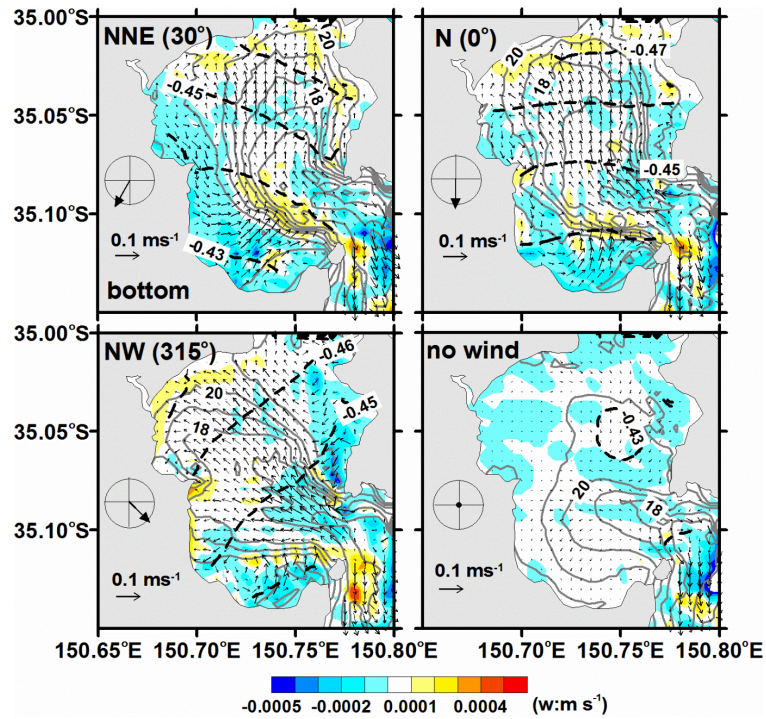


949

950 **Fig. 8.** (I) Spatial distribution of residence time with varying upwelling-favorable
 951 wind directions and a uniform wind of 0.4 N m^{-2} : (a) without wind, (b) ENE (60°), (c) NE
 952 (45°), (d) NNE (30°), (e) N (0°), and (f) NW (315°). (II) Spatial distribution of residence time
 953 with varying wind strengths and a constant upwelling-favorable wind direction of NNE (30°):
 954 (a, a') without wind, (b) 0.1 N m^{-2} , (c) 0.2 N m^{-2} , (d) 0.3 N m^{-2} , (e) 0.4 N m^{-2} , and (f) 0.5 N m^{-2} .
 955 Values higher than 15 days could not be detailed due to a two week simulation period.

956

957



958

959 **Fig. 9.** The distribution of sea level, current, and temperature on March 21, 2011 for different
 960 wind directions. The color shading represents daily depth-averaged w-velocity. The negative
 961 sign means downward flow. Grey contour lines with 1.0 $^{\circ}\text{C}$ intervals represent bottom
 962 temperature. Arrow vectors are bottom current velocity (unit: m s^{-1}). Black bold dashed lines
 963 with 0.01 m intervals denote daily-averaged sea levels. Superimposed is the wind vector with
 964 the radius of the circle indicating 0.4 N m^{-2} .

965

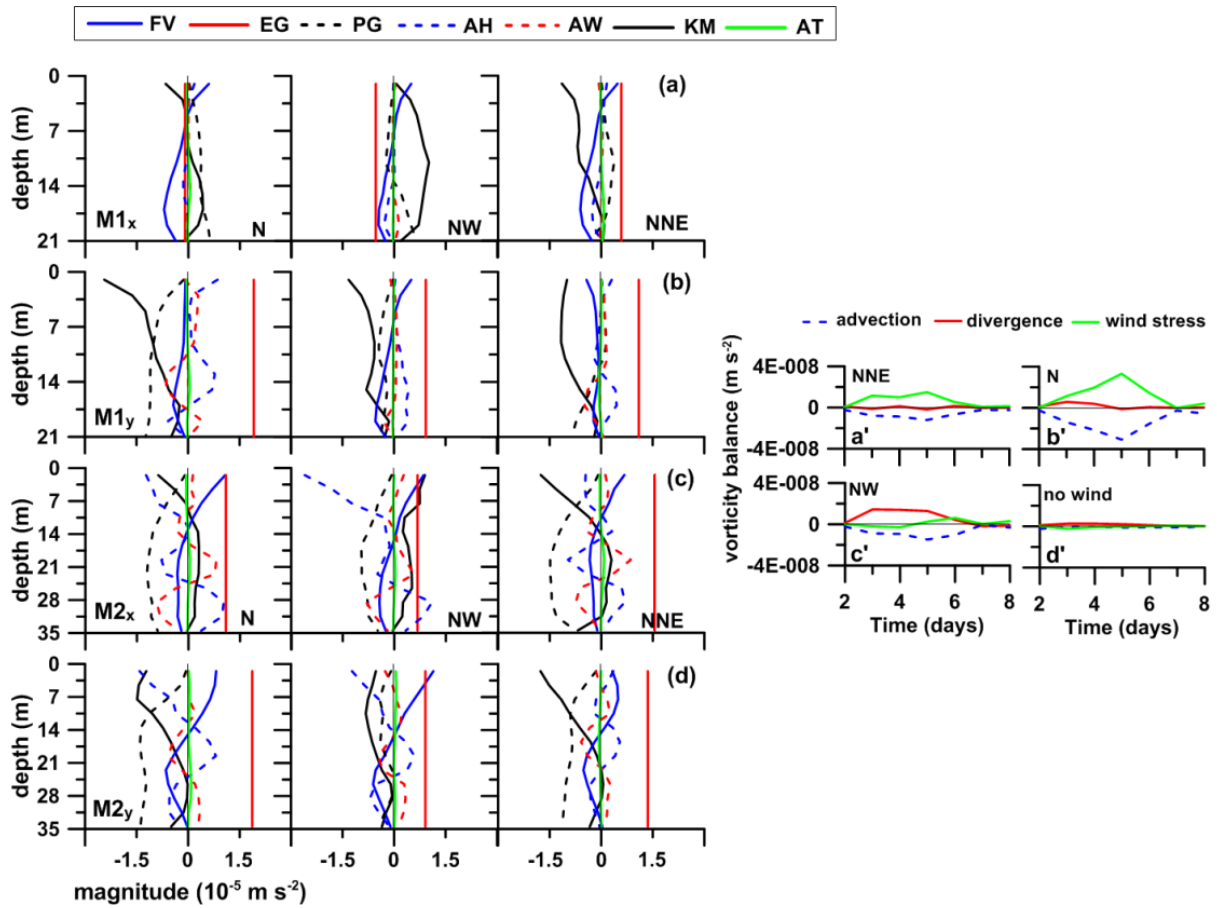
966

967

968

969

970



972

973 **Fig. 10.** Vertical profiles of daily-averaged terms of momentum equations in the eastward (a,
 974 c) and northward (b, d) directions on March 21, 2011 at sites M1 (a, b) and M2 (c, d) (see Fig.
 975 1c), for N (0°), NW (315°), and NNE (30°). Subscripts, x and y, in M1 and M2 indicate the
 976 momentum balance in the eastward and northward directions. Line colors represent the
 977 following: FV, Coriolis force; EG, surface elevation gradient; PG, baroclinic pressure
 978 gradient; AH, horizontal advection; AW, vertical advection; KM, vertical diffusion; and AT,
 979 acceleration. Vorticity balance (a'-d') of horizontally and vertically averaged circulation for
 980 NNE, N, NW and no wind forcing inside the bay.

981

982

983

984